Magma mixing in a granite and related rock association: insight from its mineralogical, petrochemical and reversed isotope features

Ding-Sheng Jiang, Xi-Sheng Xu, Yan Xia, Saskia Erdmann

AGU PUBLICATIONS

JGR

Journal of Geophysical Research: Solid Earth

RESEARCH ARTICLE

10.1002/2017JB014886

Key Points:
- Mafic rocks are more isotopically enriched than coexisting felsic rocks and thus show a "reversed isotope" feature
- Robust evidence of magma mixing is revealed by mineralogical, petrochemical, and "reversed isotope" features
- Injection of mafic magma does not necessarily imprint depleted isotopic signatures on the host felsic melt

Supporting Information:
- Supporting Information S1

Correspondence to:
X.-S. Xu,
xsxu@nju.edu.cn

Citation:
Jiang, D.-S., Xu, X.-S., Xia, Y., & Erdmann, S. (2018). Magma mixing in a granite and related rock association: Insight from its mineralogical, petrochemical, and "reversed isotope" features. *Journal of Geophysical Research: Solid Earth*, *123*, 2262–2285. https://doi.org/10.1002/2017JB014886

Received 17 AUG 2017
Accepted 3 JAN 2018
Accepted article online 7 JAN 2018
Published online 25 MAR 2018

Magma Mixing in a Granite and Related Rock Association: Insight From Its Mineralogical, Petrochemical, and "Reversed Isotope" Features

Ding-Sheng Jiang[1], Xi-Sheng Xu[1], Yan Xia[1], and Saskia Erdmann[1,2]

[1]State Key Laboratory for Mineral Deposits Research, School of Earth Sciences and Engineering, Nanjing University, Nanjing, China, [2]Now at Université d'Orléans–CNRS/INSU–ISTO–BRGM, UMR 7327, Orléans, France

Abstract Magma mixing commonly takes place between isotopically depleted mafic and enriched felsic magmas. Here we present isotopic evidence exhibiting the opposite behavior in the Early Cretaceous Siling complex (south China), which is composed of gabbro, quartz diorite, granodiorite, and alkali feldspar granite with locally many mafic microgranular enclaves. Field observations and zircon U-Pb dating indicate that all of the rock units crystallized contemporaneously at ca. 127–129 Ma. Mineralogical and petrochemical analyses indicate that the Siling quartz diorite and granodiorite crystallized from hybrid magmas of temporally and spatially coexisting gabbroic and granitic melts. The Siling gabbro, characterized by variable yet enriched Sr-Nd-Hf isotopic compositions [$(^{87}Sr/^{86}Sr)_i$ = 0.70788 to 0.70833; $\varepsilon_{Nd}(t)$ = −7.6 to −3.5; $\varepsilon_{Hf}(t)$ = −6.8 to −1.9], exhibits Th/Nb, Nb/Nb*, and Sm/Yb versus $\varepsilon_{Nd}(t)$ correlations, indicating that the gabbro represents variable mixing of magmas derived from deep-level pyroxenite and shallow-level peridotite sources. The Siling alkali feldspar granite, which has typical A-type characteristics, exhibits less enriched Sr-Nd-Hf isotopic signatures [$(^{87}Sr/^{86}Sr)_i$ = 0.70650; $\varepsilon_{Nd}(t)$ = −3.2 to −2.5; $\varepsilon_{Hf}(t)$ = −1.3] than the coexisting gabbro, indicating its derivation from the remelting of juvenile lower crust. "Reversed isotope" feature of the Siling gabbro and alkali feldspar granite means that the quartz diorite and granodiorite recorded "reversed isotope" mixing between isotopically enriched mafic and relatively depleted felsic magmas. The results indicate that the injection of mantle-derived mafic magma does not necessarily imprint relatively depleted isotopic signatures on the host felsic melt and that the vertical growth of the continental crust by the input of isotopically enriched magma should be concerned.

1. Introduction

Magma mixing between mafic and felsic melts is a common open-system process (e.g., Barbarin, 2005; Gagnevin et al., 2007, 2011; Griffin et al., 2002; Laumonier et al., 2014; Plail et al., 2018; Słaby & Martin, 2008; Ubide et al., 2014). Where macroscale evidence of magma mixing persists, isotopically depleted mafic magma in the form of syn-plutonic dykes or mafic microgranular enclaves (MMEs), and enriched felsic melt in the form of the host granitoids, are commonly identified (e.g., Cheng et al., 2012; Clemens & Stevens, 2016; Luo et al., 2015; Słaby & Martin, 2008; Zhang et al., 2016). In some examples, where the recharged and resident magmas have been thoroughly mixed, all macroscale evidence of mixing and whole-rock isotope heterogeneity may be obliterated (e.g., Appleby et al., 2008; Gagnevin et al., 2011; Griffin et al., 2002; Luo et al., 2015; Yang et al., 2013). Mixing of isotopically depleted mafic magma and enriched felsic magma is usually considered (e.g., Słaby & Martin, 2008; Stelten et al., 2013; Ubide et al., 2014; Zhang et al., 2016), resting on the assumption that mantle-derived mafic magmas are more isotopically depleted than crust-derived felsic melts (Barbarin, 2005; Cheng et al., 2012; Clemens & Stevens, 2016; Griffin et al., 2002; Słaby & Martin, 2008).

Isotopically enriched mafic rocks have, however, been identified in the North China Craton (e.g., Ma et al., 2014; Yang et al., 2004) and in the Pitcairn and Samoan islands (e.g., Eisele et al., 2002; Jackson et al., 2007), while isotopically depleted granitic rocks have been identified in the Central Asian Orogenic Belt (e.g., Jahn et al., 2000; Jahn, 2004; Wang et al., 2009) and in the Gangdese batholith (Tibet) (e.g., Chu et al., 2006; Chung et al., 2009). In some cases, intrusive or volcanic suites ranging from mafic through intermediate to felsic rocks show a trend of decreasing $(^{87}Sr/^{86}Sr)_i$ ratios and increasing $\varepsilon_{Nd}(t)$ and $\varepsilon_{Hf}(t)$ values, along with increasing whole-rock SiO_2 contents; that is, they show a "reversed isotope" character (Table 1; e.g., Coleman et al., 1992; Ratajeski et al., 2001; Su et al., 2011; Tomlinson et al., 2002; Xiang et al., 2017; Zhong et al., 2011). Systems with such reversed isotope characters commonly display clear evidence of magma mixing (e.g.,

Table 1
Examples of Reversed Isotope Rock Suites Worldwide

Pluton name	Location	Rock type	Age(Ma)	Whole rock $(^{87}Sr/^{86}Sr)_i$	Whole rock $\varepsilon_{Nd}(t)$	$\varepsilon_{Hf}(t)$	Reference
Lamarck intrusive suite	Sierra Nevada batholith, California	Gabbro	90	0.70631–0.70656	− 5.63 to − 4.20		Coleman et al. (1992)
		Diorite	90	0.70633–0.70641	− 4.75 to − 4.33		
		Granodiorite	90	0.70619–0.70658	− 4.62 to − 2.91		
Yosemite Valley intrusive suite		Diorite	103.5 ± 0.2	0.707089–0.707729	− 6.22 to − 5.30		Ratajeski et al. (2001)
		Intermediate-silicic rocks	103	0.706691–0.706927	− 4.80 to − 4.46		
		Granite	103	0.706548–0.706567	− 4.62 to − 4.40		
Tommyhow Lake area	Obonga Lake greenstone belt, western Superior Province	Basalt	2726–2732		0.31		Tomlinson et al. (2002)
		Dacite			1.35		
		Rhyolite			2.12		
Gouldsboro Pluton	Coastal Maine Magmatic Province	Low-K enclave	419	0.70486–0.70555	1.11 to 1.98		Waight et al. (2007)
		Granite	419	0.70505–0.70512	2.83 to 3.11		
Hongshishan intrusion	Beishan region, Central Asian Orogenic Belt	Diorite	279.1 ± 2.9	0.71012	1.8	0.8 to 7.8 [a]	Su et al. (2011)
		Rhyolite	279.7 ± 4.8	0.70644–0.70663	2.6 to 4.3	0.3 to 8.5 [a]	
Baima Complex	Emeishan large igneous province, China	Gabbro	258.2 ± 2.2		− 1.17		Zhong et al. (2011)
		Basaltic enclave	259.0 ± 3.1		− 0.71 to 0.32		
		Fayalite syenite	258.5 ± 2.3		1.55		
		Quartz syenite	257.8 ± 2.6		2.93		
Panzhihua Complex		Gabbro	257.9 ± 2.4		0.93	4.08 [a]	
		Syeno-diorite	259.5 ± 1.1		2.01 to 2.58	7.35 to 8.44 [a]	
		Syenite	255.8 ± 1.8		2.65	7.62 [a]	
Linghshan pluton	Gan-Hang Belt (south China)	MME	129.1± 2.3		− 3.9 to − 3.0	− 2.7 to − 1.7 [b]	Xiang et al. (2017)
		Biotite granite	133.7 ± 1.1		− 3.4 to − 0.32	− 2.5 to − 0.48 [b]	
		Albite granite	133.6 ± 2.5		− 0.29	− 0.32 [b]	

[a]Refers to $\varepsilon_{Hf}(t)$ values for whole rock. [b]Refers to $\varepsilon_{Hf}(t)$ values for zircons.

Coleman et al., 1992; Ratajeski et al., 2001; Xiang et al., 2017; Zhong et al., 2011). Waight et al. (2007) and Zhong et al. (2011) have reported two cases in which MMEs are more isotopically enriched than their granitic and syenitic hosts (Table 1).

This study documents an example of reversed isotope magma mixing in the Cretaceous Siling complex exposed in the Gan-Hang Belt, South China. Detailed field and petrographic observations, mineralogical and whole-rock elemental and isotopic analyses, and zircon U-Pb dating were carried out to characterize the ages, sources, and evolution of the gabbroic to granitic components. The results show that the isotopically relatively depleted felsic melt was recharged by and mixed with isotopically enriched mafic magma. The study highlights that reversed isotope magma mixing should be considered for all well-mixed magma systems, where cryptic, mineral-scale evidence may persist.

2. Geological Setting and Petrography

The South China Block, which hosts the studied complex, is composed of two major blocks: the Yangtze block to the northwest and the Cathaysia block to the southeast (Figure 1a). These two blocks amalgamated during the Neoproterozoic along the Jiangshan-Shaoxing Fault to form the Jiangnan Orogeny (Li et al., 2008, 2009; Wang et al., 2008a; Xia et al., 2015, 2017). In Late Mesozoic, voluminous magmatism in the South China Block built a ~600 km wide belt of volcanic-intrusive complexes (Zhou et al., 2006; Zhou & Li, 2000). The magmatism is suggested to have been related to the subduction of the Paleo-Pacific plate toward the Eurasia continent (Li & Li, 2007; Li et al., 2007; Sun et al., 2007; Zhou et al., 2006; Zhou & Li, 2000). Most studies have inferred that basaltic underplating played a key role in large-scale crustal partial melting (He & Xu, 2012; Liu et al., 2012, 2014; L. Liu et al., 2015; Zhou et al., 2006; Zhou & Li, 2000).

Late Mesozoic A-type granites, including the ones studied here, were emplaced along four major fault zones known as low-Nd-model-age belts (Gilder et al., 1991): the Nanling Belt, the Xiangguiyue Belt, the Gan-Hang Belt, and the Southeastern Coast Belt. The Siling complex forms part of the northeast Gan-Hang Belt (GHB), which extends for more than 450 km in a NNE-SSW direction (Figure 1a). Extensive extrusive and intrusive

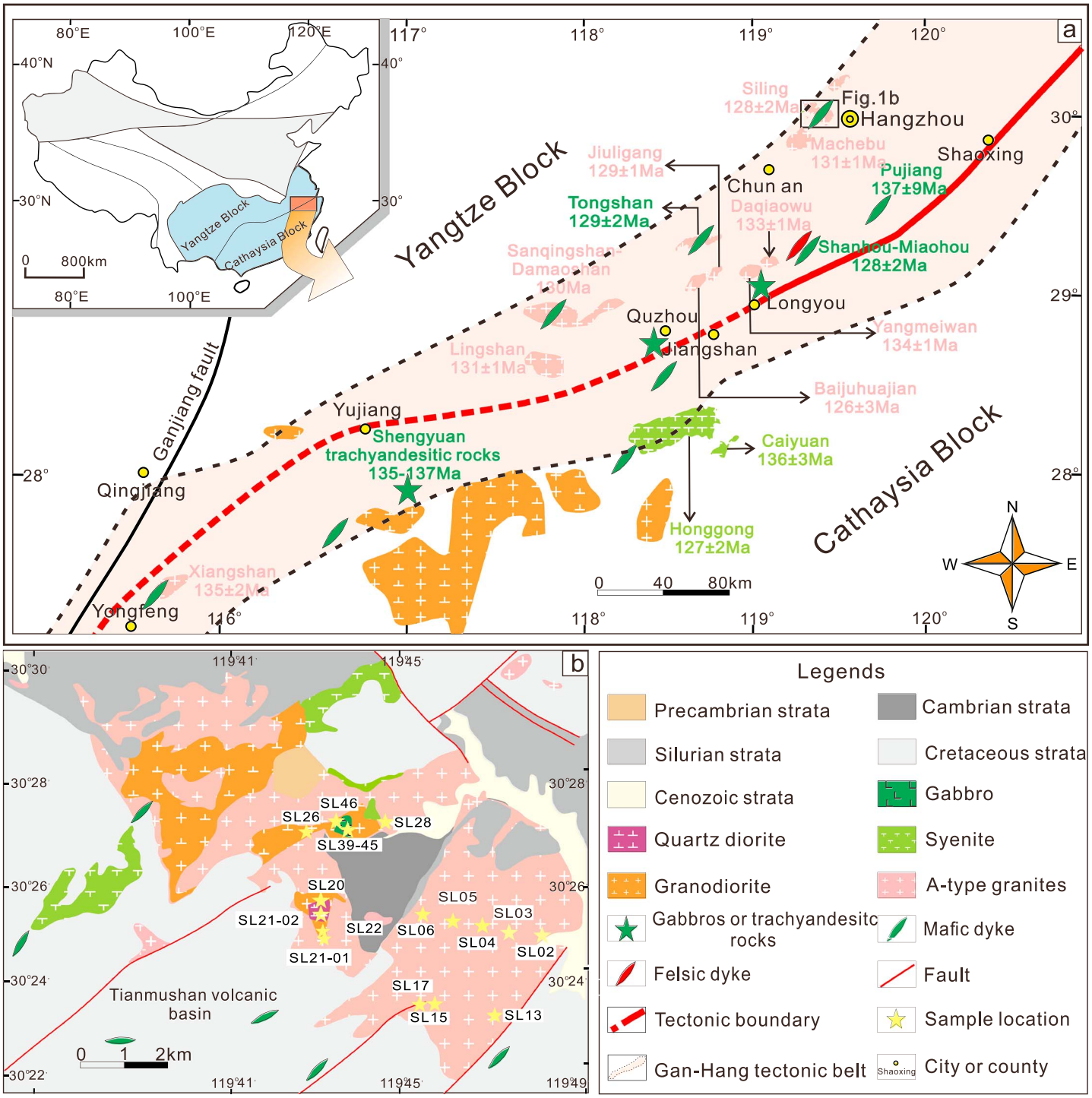

Figure 1. (a) Schematic map showing the distribution of Yanshanian (136–126 Ma) intrusions in the GHB, South China (modified after Yu et al., 2004). (b) Geological map of the Siling complex modified after Geological Bureau of Zhejiang Province (1967). Age data for coeval mafic rocks are from Jiang et al. (2011), Qi et al. (2012, 2016), Shu et al. (2017), and Xia et al. (2016). The coeval A-type granites age data are from Hu et al. (2017), Jiang et al. (2005, 2011), Li et al. (2013), Sun et al. (2015), Wong et al. (2009), Xia et al. (2016), Yang et al. (2012), and Zhou et al. (2013). The indicated ages of syenitic rocks are from He and Xu (2012).

magmatic activity occurred in the GHB during the Early Cretaceous for available Ar-Ar, K-Ar, and zircon U-Pb data defining an age peak at ca. 130 Ma (Hu et al., 2017; Jiang et al., 2005, 2011; Peng et al., 2004; Qi et al., 2012, 2016; Shu et al., 2017; Sun et al., 2015; Wong et al., 2009; Xia et al., 2016; Xiang et al., 2017; Yang et al., 2012; L. Zhao et al., 2016; Zhou et al., 2013). The mafic magmatic rocks in the GHB are characterized

by variable isotopic compositions [$(^{87}Sr/^{86}Sr)_i$ = 0.70354–0.71086; $\varepsilon_{Nd}(t)$ = −10.4 to +6.6; Table S6 in the supporting information; Jiang et al., 2011; Qi et al., 2012, 2016; Shu et al., 2017; Xia et al., 2016]. Some granitic rocks contain MMEs (e.g., the Tonglu and Xiangshan complexes, and the Lingshan and Baijuhuajian granites), indicating the injection of juvenile mantle-derived components during their formation (Griffin et al., 2000; Jiang et al., 2005; Wong et al., 2009; Xiang et al., 2017; Zhou et al., 2013).

The Siling complex located in the GHB crops out northwest of Hangzhou City, where it is exposed over an area of ~100 km^2 (Figure 1b; Geological Bureau of Zhejiang Province, 1967). The complex intrudes Sinian and Ordovician metasediments and Lower Cretaceous volcanic strata and is lithologically diverse, containing granite, granodiorite, subordinate quartz diorite, and gabbro. A prominent feature of the Siling complex is that it contains many enclaves in the granodiorite and alkali feldspar granite.

2.1. Siling Gabbros

The Siling gabbros, located in the central area of the complex, are massive and medium- to coarse-grained. Many millimeter-scale granite back-veins are developed within the gabbro (Figure 2a). The mineral assemblage of the massive gabbros is dominated by plagioclase (55 vol.%), amphibole (35 vol.%), clinopyroxene (5 vol.%), orthopyroxene (2 vol.%), and accessory magnetite, ilmenite, titanite, and apatite. The abundance of amphibole is a notable feature of the gabbros (Figure 2b).

2.2. Siling Quartz Diorites and Granodiorites

Quartz diorites, and more commonly granodiorites, form irregular bodies with maximum dimensions of up to ~5 km, with diffuse contacts between them. The quartz diorites are typically fine- to medium-grained and are composed of plagioclase (55 vol.%), K-feldspar (12 vol.%), amphibole (10 vol.%), quartz (10 vol.%), clinopyroxene (5 vol.%), and biotite (3 vol.%). Accessory minerals include titanite, apatite, zircon, and magnetite. The Siling granodiorites are mostly porphyritic and are characterized by euhedral plagioclase (20 vol.%), K-feldspar (10 vol.%), and minor quartz (5 vol.%) phenocrysts in a matrix of 30 vol.% plagioclase, 12 vol.% quartz, 8 vol.% K-feldspar, 5 vol.% amphibole, and 5 vol.% biotite, with accessory zircon, titanite, apatite, and Fe-Ti oxides. Rapakivi K-feldspar phenocrysts with plagioclase mantles, poikilitic quartz phenocrysts with K-feldspar mantles (Figure 2c), and plagioclase or quartz phenocrysts rimmed by biotite are common.

Enclaves in the Siling granodiorite and alkali feldspar granite are typically fine-grained and equigranular to porphyritic. They are dark gray in color and range in size from $<$5 cm to $>$10 cm in the longest dimension (Figure 2d). The enclaves are mostly ellipsoid-ovoid, with sharp to diffuse contacts with their hosts. These enclaves contain the same mineral assemblages as their hosts but with more abundant amphibole, biotite, plagioclase, and euhedral, acicular apatite (Figures 2e and 2f) and less K-feldspar. Partially resorbed plagioclase and ocellar quartz xenocrysts (quartz rimmed by biotite; Figure 2g) are common constituents.

2.3. Siling Alkali Feldspar Granites

The Siling alkali feldspar granites, the main lithology of the Siling complex, are massive, fine- to medium-grained, and pale red in color. Their mineral assemblage is composed of perthitic K-feldspar (55 vol.%), quartz (30 vol.%), plagioclase (5 vol.%), and interstitial biotite (5 vol.%). Accessory minerals include zircon, apatite, monazite, allanite, fluorite, and Fe-Ti oxides. Fluorite aggregates (Figure 2h) and micrographic intergrowths of quartz and alkali feldspar (Figure 2i) are common.

3. Sampling and Analytical Methods

After petrographic examination, 22 fresh representative samples were selected, and their locations are shown in Figure 1b. All gabbro samples were collected from the center of the stock to minimize any effects of contamination by granitic material (i.e., by back-veins that are present near the external contact of the stock and/or diffusive exchange between gabbro and alkali feldspar granite). Samples with visible plagioclase and ocellar quartz xenocrysts were avoided when enclaves were selected for geochemical analyses. To characterize end-member compositions and magma mixing in the Siling complex, whole-rock and mineral-scale (zircon, plagioclase, biotite) major- and trace-element and isotopic composition analyses were carried out.

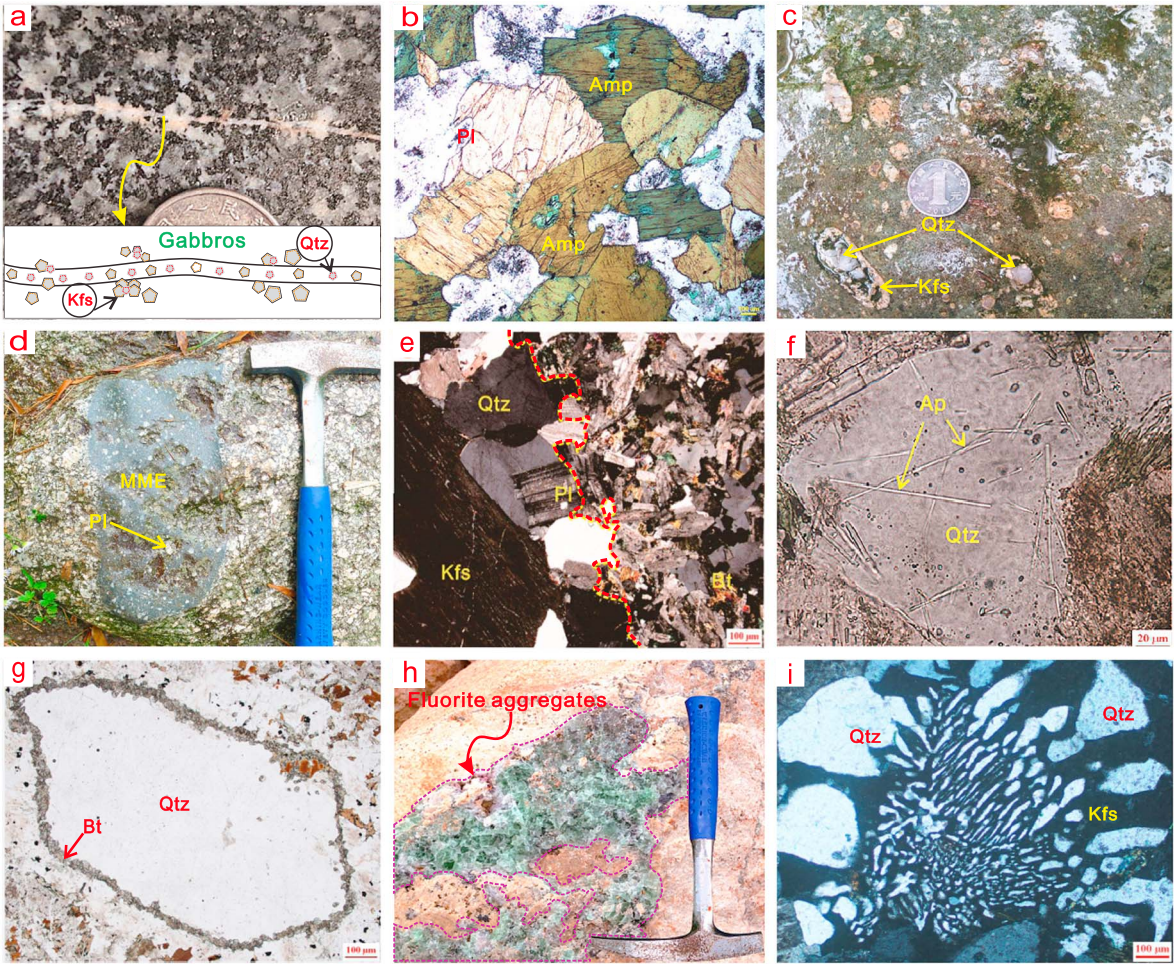

Figure 2. Representative field photographs and microphotographs of the Siling complex. (a) Millimeter-scale granite back-veins in the marginal massive gabbro. (b) Abundant amphibole crystals in the Siling gabbro. (c) Quartz with K-feldspar mantles in the Siling granodiorite. (d) Granodiorite with a dioritic magmatic enclave and enclosed plagioclase xenocrysts. (e) Typical mineral assemblages in the alkali feldspar granite (left) and a granodioritic MME (right). (f) Apatite displays a euhedral acicular habit in the MME. (g) Quartz rimmed by biotite in the dioritic MME. (h) Fluorite aggregates in the Siling alkali feldspar granite. (i) Granophyric texture of the Siling alkali feldspar granite. Mineral abbreviations: Amp, amphibole; Ap, apatite; Bt, biotite; Kfs, K-feldspar; MME, mafic microgranular enclave; Pl, plagioclase; Qtz, quartz.

3.1. Electron Microprobe Analyses of Biotite and Plagioclase

The compositions of biotite and plagioclase were determined at the State Key Laboratory for Mineral Deposits Research, Nanjing University, using a JEOL JXA-8100 electron microprobe. The analyses were carried out at a 20 kV accelerating voltage, a 20 nA beam current, and with a focused (nominal 1 μm) beam. Mineral standards were natural amphibole (Al, Mg, Ca, Na, and K), fayalite (Si, Fe, and Mn), and synthetic TiO_2 (Ti). Matrix effects were automatically corrected using the ZAF software provided by JEOL.

3.2. Zircon U-Pb Dating

Zircon grains were separated by conventional magnetic and density techniques to determine U-Pb ages and Hf isotope composition. Internal textures of all zircon crystals were characterized by cathodoluminescence (CL) microscopy, obtained using a JEOL JSM-7000F scanning electron microscope at Nanjing Hongchuang Geological Technology Co. Ltd.

Zircon U-Pb dating was carried out using an Agilent 7500a inductively coupled plasma–mass spectrometry (ICP-MS) coupled to a New Wave Research 213 nm laser ablation system at the State Key Laboratory for Mineral Deposits Research, Nanjing University. Analyses were acquired at a beam diameter of 32 μm, a 5 Hz repetition rate, and an energy of 10–20 J/cm^2. Homogeneous zircon GEMOC GJ-1 ($^{207}Pb/^{206}Pb$ age of

608.5 ± 0.4 Ma and $^{206}Pb/^{238}U$ age of 599.8 ± 4.5 Ma; Jackson et al., 2004) was used as an external standard for mass bias and instrument drift correction (analyzed twice every 10 analyses). The Mud Tank zircon standard was used as an independent control (analyzed once every 10 analyses), which yielded a weighted mean $^{206}Pb/^{238}U$ age of 728 ± 6 Ma (2σ; MSWD = 0.69), which is consistent with the age determined by isotope dilution-thermal ionization mass spectrometer (732 ± 5 Ma; Black & Gulson, 1978).

3.3. Zircon Hf-Isotope Analysis

In situ Lu-Hf isotopic analysis of zircon was performed on the same grains and on the same or centrally symmetrical domains that were analyzed for U-Pb age dating. The analyses were carried out using a Neptune Plus Multicollector (MC)-ICP-MS attached to a New Wave ArF 193 nm laser ablation system at the State Key Laboratory for Mineral Deposits Research, Nanjing University. Zircon standard 91500 was analyzed to evaluate the reliability of the analyses, which yielded a weighted mean $^{176}Hf/^{177}Hf$ ratio of 0.282296 ± 8 (2σ; MSWD = 0.58; Goolaerts et al., 2004). The obtained $^{176}Lu/^{177}Hf$ ratios and the ^{176}Lu decay constant of 1.867×10^{-11} yr^{-1} (Söderlund et al., 2004) were used to calculate initial $^{176}Hf/^{177}Hf$ ratios. The chondritic values of $^{176}Lu/^{177}Hf$ = 0.0336 ± 1 and $^{176}Hf/^{177}Hf$ = 0.282785 ± 11(2σ; Bouvier et al., 2008) were used for calculating ε_{Hf} values. The depleted mantle Hf model ages (T_{DM}) were calculated using the measured $^{176}Lu/^{177}Hf$ ratios, referred to a model depleted mantle with a present-day $^{176}Hf/^{177}Hf$ = 0.283250 and with $^{176}Lu/^{177}Hf$ = 0.0384 (Griffin et al., 2000). Two-stage Hf model ages (T_{DM2}) were calculated by assuming a mean $^{176}Lu/^{177}Hf$ value of 0.015 for the average continental crust (Griffin et al., 2002).

3.4. Whole-Rock Major and Trace Element Analysis

Whole-rock major-element compositions were determined using a Thermo Scientific ARL9800XP + X-ray fluorescence spectrometer with a 50 kV accelerating voltage and a beam current of 50 mA at the State Key Laboratory for Mineral Deposits Research, Nanjing University. For major-element analyses, mixtures of whole-rock powders (0.5 g) and $Li_2B_4O_7$ + $LiBO_2$ + LiBr (11 g) were fused into glass disks. Loss on ignition (LOI) was determined by ignition at 1100°C for 10 h on 2 g of powder. Standard GSR-3 was used to monitor the analytical accuracy.

Trace element analysis of whole rocks was carried out at Nanjing FocuMS Technology Co. Ltd. About 40 mg powder was mixed with 0.5 mL HNO3 and 1.0 mL HF in high-pressure PTFE bombs. These bombs were steel-jacketed and placed in the oven at 195°C for 48 h for mafic samples and 72 h for felsic samples. Rock digestion diluent was nebulized into Agilent Technologies 7700x quadrupole ICP-MS (Hachioji, Tokyo, Japan) to determine the trace element abundances. Deviation were better than ±10% for elements exceeding 10 ppm and better than ±5% for elements exceeding 50 ppm.

3.5. Whole-Rock Sr-Nd-Hf Isotope Analysis

Whole-rock Sr and Nd-Hf isotopes were measured using a Finnigan Triton TI thermal ionization mass spectrometer and a Neptune (Plus) MC-ICP-MS, respectively, at the State Key Laboratory for Mineral Deposits Research, Nanjing University, following the methods of Pu et al. (2005) and Yang et al. (2010). The Sr-Nd-Hf isotope compositions were normalized to $^{86}Sr/^{88}Sr$ = 0.1194, $^{146}Nd/^{144}Nd$ = 0.7219, and $^{179}Hf/^{177}Hf$ = 0.7325, respectively. During the analyses, every 10-sample analyses were followed by one standard measurement. Standards NBS-987, Jndi-1, and JMC-475 were used for Sr, Nd, and Hf isotopic measurements, respectively. Measured $^{87}Sr/^{86}Sr$ values for NBS-987, $^{143}Nd/^{144}Nd$ values for Jndi-1, and $^{176}Hf/^{177}Hf$ values for JMC-475 were 0.710248 ± 0.000004 (2σ), 0.512095 ± 0.000008 (2σ), and 0.282151 ± 0.000009 (2σ), respectively.

4. Results

4.1. Mineral Compositions

Biotites in the Siling alkali feldspar granite are annite-rich with X_{Fe} values [$Fe^t/(Fe^t + Mg)$] of 0.67–0.69, and they are F-rich (2.8–3.3 wt.%; Table S1).

Representative plagioclase compositions of Siling quartz diorite and granodiorite are listed in Table S2 and illustrated in Figure 3. Plagioclase crystals in the more evolved Siling granodiorite sample (SL26) are texturally simple and of relatively homogeneous composition. They have an andesine composition (~$An_{32–44}$) with weak normal zoning. Plagioclase crystals in the quartz diorite and less-evolved granodiorite (SL46),

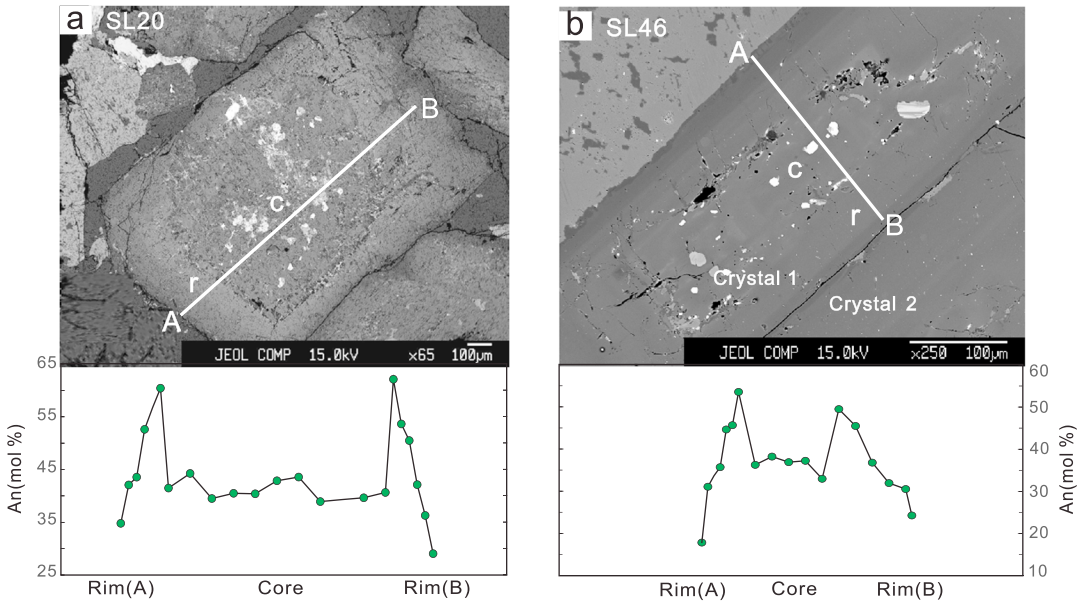

Figure 3. (a) Backscattered-electron (BSE) images and geochemical profiles of plagioclase crystals in the Siling quartz diorite (crystal I) and (b) the less-evolved granodiorite. Some plagioclases in the Siling quartz diorite and the less-evolved granodiorite show remarkable core-rim zoning with sieve-textured low-An cores (labeled "c") and high-An rim zones (labeled "r"), separated by a resorption surface.

however, exhibit prominent core-rim zoning (Figures 3a and 3b) and commonly display sieve textures with abundant K-feldspar, biotite, and Fe-Ti oxide inclusions. The sieve-textured plagioclase cores in the quartz diorite and less-evolved granodiorite have andesine compositions (~$An_{32–46}$ and ~$An_{33–38}$, respectively), comparable with those of plagioclases in the more-evolved granodiorite. Rim zones in the sieve-textured plagioclase are more calcic, with labradorite to andesine compositions ($An_{29–64}$ and $An_{18–54}$, respectively; Figures 3a and 3b).

4.2. Zircon U-Pb Dating

Zircons in the dioritic MME (sample SL21) and quartz diorite (SL20) are moderately bright and prismatic in CL images, with weak oscillatory zoning (Figure 4f). Twenty spot analyses of zircons from the dioritic MME gave a weighted mean $^{206}Pb/^{238}U$ age of 128 ± 1 Ma (MSWD = 0.44; Figure 4a). Twenty-two spot analyses of zircons from the quartz diorite gave a weighted mean $^{206}Pb/^{238}U$ age of 127 ± 1 Ma (MSWD = 0.16; Figure 4b).

Zircons in the granodiorite show significant core-rim zoning in CL (Figure 4f). The rims are gray while the cores are black. For one sample (SL46), analyses of 34 crystals yielded a weighted mean $^{206}Pb/^{238}U$ age of 129 ± 1 Ma (MSWD = 0.10; Figure 4c). Zircons in the alkali feldspar granite are typically dark in CL, with pronounced oscillatory zoning (Figure 4f). For two samples (SL03, SL05), analyses of 17 grains from each yielded weighted mean $^{206}Pb/^{238}U$ ages of 129 ± 1 Ma (MSWD = 0.61; Figure 4d) and 129 ± 1 Ma (MSWD = 0.66; Figure 4e), respectively.

4.3. Zircon Hf Isotopic Compositions

Results of in situ analyses of Lu-Hf isotopes in zircons are given in Table 2 and Table S4 and illustrated in Figures 4f and 5. Zircon $\varepsilon_{Hf}(t)$ values range from −6.5 to −2.5 in dioritic MME and from −7.0 to +0.5 in quartz diorite, with weighted means of −4.2 ± 0.6 and −4.5 ± 0.6, respectively. Zircons from the Siling granodiorite and alkali feldspar granite exhibit less enriched Hf isotopic compositions with $\varepsilon_{Hf}(t)$ values of −6.1 to +0.8 and −3.4 to +4.0, with weighted means of −2.3 ± 0.6 and −1.2 ± 0.7, respectively.

4.4. Whole-Rock Major- and Trace-Element Compositions

The Siling gabbros have low SiO_2 (45–47 wt.%), high K_2O (1.5–2.5 wt.%), and high K_2O/Na_2O ratios (0.5–1.2). They are classified as shoshonitic and potassic (Figures S1a and S1b; Foley et al., 1987; Peccerillo & Taylor, 1976). They also have relatively high MgO contents (6.0–6.7 wt.%) but have low Mg numbers

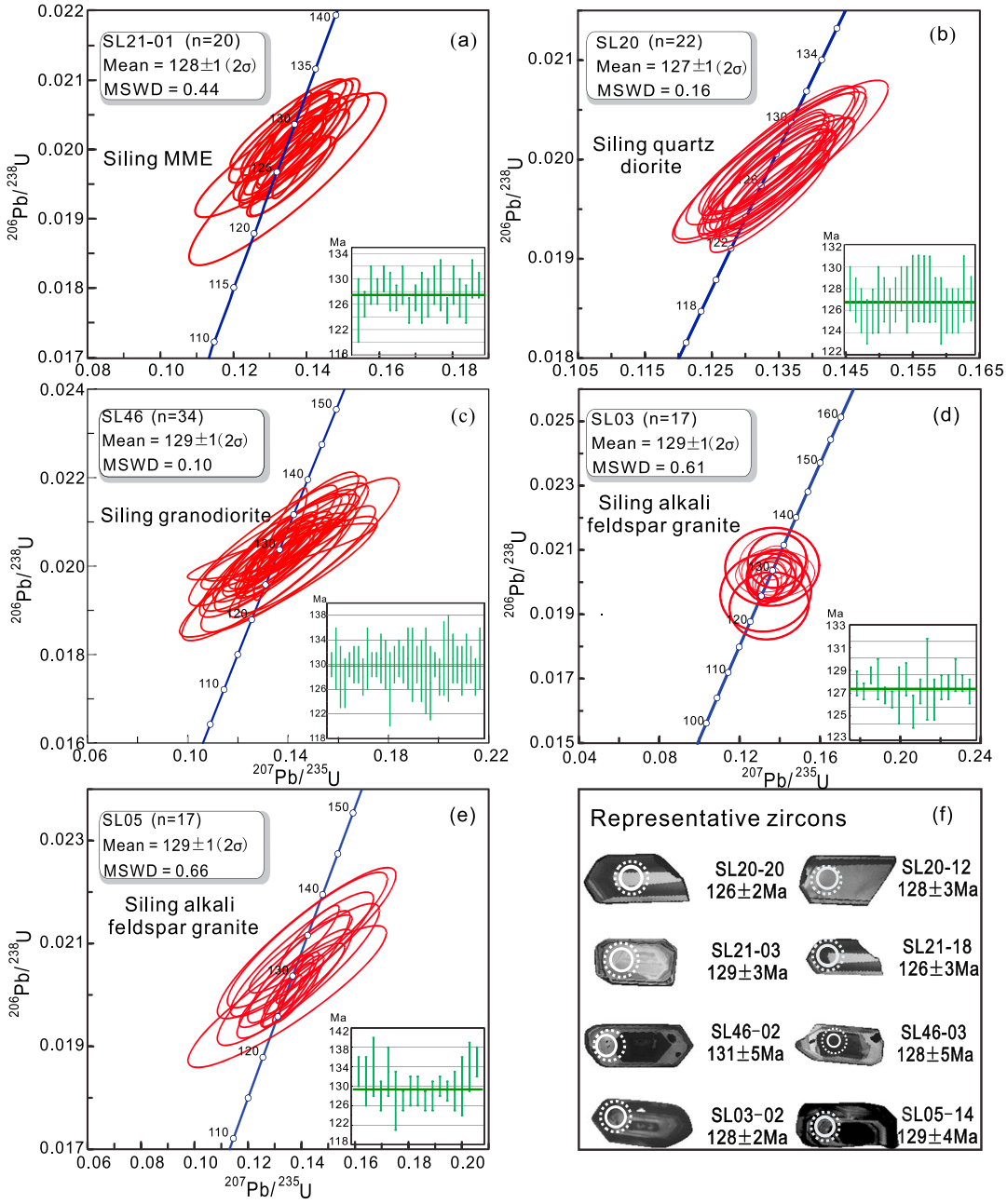

Figure 4. Zircon U–Pb concordia plots with weighted mean $^{206}Pb/^{238}U$ ages for the Siling complex: (a) dioritic MME; (b) quartz diorite; (c) granodiorite; and (d, e) granite samples. All age data are within error (±1 Ma) of each other at 127–129 Ma. (f) CL images of representative zircons from the Siling complex. The small solid circles indicate the location of points for LA–ICPMS U–Pb dating. The large dashed circles indicate the location of LA–MC–ICPMS Hf isotopic analyses. Note that relict zircon cores (Figure 4f) in the Siling granodiorite (e.g., SL46–03) have age similar to the rims (e.g., SL46–02).

[$Mg^{\#}$ = 30–32; $Mg^{\#}$ = 100 × MgO/(MgO + FeO_t)], reflecting their high Fe contents (FeO_t = 13.1–14.9 wt.%). They display a relative enrichment in light-rare-earth-elements (LREE) over heavy-rare-earth-elements (HREEs), with weakly negative Eu anomalies (Eu/Eu* = 0.82–0.87; Figure S2e; Taylor & McLennan, 1985). The Siling gabbros also have high contents of large-ion lithophile elements (LILE; Rb, K, and Pb), with significant negative Nb-Ta anomalies (Figure S2f; McDonough & Sun, 1995).

The quartz diorites and granodiorites have SiO_2 and total-alkali contents of 59–67 wt.% and 7.1–7.8 wt.%, respectively. Enclaves in the granodiorite and alkali feldspar granite are respectively dioritic and

Table 2
In Situ Zircon and Whole-Rock Hf Isotopic Data for the Quartz Diorites, Dioritic MMEs, Granodiorites, and Alkali Feldspar Granites From the Siling Complex

Sample	Lithology	Age (Ma)	In situ zircon analysis					Whole-rock analysis						
			Number	$(^{176}Hf/^{177}Hf)_i$	$\varepsilon_{Hf}(t)$	Weighted values	T_{DM2} (Ga)	Lu (ppm)	Hf (ppm)	$^{176}Lu/^{177}Hf$	$^{176}Hf/^{177}Hf$	$^{176}Hf/^{177}Hf_{(i)}$	$\varepsilon_{Hf}(t)$	T_{DM2}(Ga)
SL03	Granite	129 ± 1	17	0.282622–0.282766	−3.5 to +2.2	−1.2 ± 0.7	1.02–1.38	1.16	7.16	0.0230	0.282711 ± 4	0.282656	−1.3	1.26
SL05		129 ± 1	17	0.282611–0.282847	−3.4 to +4.0	−1.2 ± 0.7	0.90–1.37							
SL46	Granodiorite	129 ± 1	34	0.282533–0.282788	−6.1 to +0.8	−2.3 ± 0.6	1.10–1.54	0.42	4.77	0.0126	0.282647 ± 5	0.282617	−2.7	1.35
SL21	Dioritic MME	128 ± 1	20	0.282522–0.282634	−6.5 to −2.5	−4.2 ± 0.6	1.31–1.56	0.47	6.44	0.0103	—	—	—	—
SL20	Quartz diorite	127 ± 1	22	0.282507–0.282717	−7.0 to +0.5	−4.5 ± 0.6	1.13–1.60	0.42	6.27	0.0096	—	—	—	—
SL40	Gabbro	ca. 128	—	—	—	—	—	0.38	2.60	0.0209	0.282688 ± 1	0.282638	−1.9	1.30
SL41			—	—	—	—	—	0.34	2.53	0.0189	0.282663 ± 3	0.282618	−2.6	1.35
SL42			—	—	—	—	—	0.32	2.22	0.0202	0.282577 ± 4	0.282529	−5.8	1.55
SL43			—	—	—	—	—	0.37	2.50	0.0209	0.282627 ± 3	0.282577	−4.1	1.44
SL44			—	—	—	—	—	0.31	2.38	0.0186	0.282545 ± 3	0.282501	−6.8	1.61
SL45			—	—	—	—	—	0.37	2.91	0.0179	0.282663 ± 2	0.282620	−2.6	1.34

granodioritic in composition. All these rocks are predominantly classified as alkaline (Figure S1c; Wright, 1969) and are metaluminous to strongly peraluminous (Figure S1d), with A/CNK ratios of 0.82–1.26. In chondrite-normalized REE diagrams, they are characterized by moderate enrichment in LREE and nearly flat HREE, with moderately negative Eu anomalies (Eu/Eu* = 0.64–0.78; Figures S2a and S2c). They exhibit enrichment in LILE and moderate to pronounced negative anomalies in high-field strength elements (HFSE), including Ti, Nb, and Ta (Figures S2b and S2d).

The Siling alkali feldspar granites are characterized by high SiO_2 (70–77 wt.%) and total alkali contents (~8.3–9.8 wt.%) and are thus classified as alkaline (Figure S1c). They contain 0.98–2.01 wt.% FeO_t and <0.3 wt.% MgO and are therefore classified as ferroan ($Fe^{\#}$ = 0.88–0.95). They are metaluminous to weakly peraluminous (A/CNK = 0.96–1.04; Figure S1d) and are characterized by typical seagull REE patterns (Figure S2e) marked by flat HREE and moderately steep LREE, with significantly negative Eu anomalies (Eu/Eu* = 0.02–0.41). They display enrichment in HFSE (Th, U, Zr, and Hf), Rb, and Pb; depletion in Ba, Sr, Eu, P, and Ti; and weakly negative Nb-Ta anomalies (Figure S2f).

Overall, the Siling gabbros, quartz diorites, granodiorites, and alkali feldspar granites define coherent and linear geochemical trends for most selected major and trace elements (Figure S3).

4.5. Whole-Rock Sr-Nd-Hf Isotopes

Whole-rock Sr-Nd-Hf isotopic compositions for the Siling complex are listed in Tables 2 and 3 and illustrated in Figure 6. For the Siling gabbros, $^{87}Sr/^{86}Sr$ ratios are 0.70853–0.70889 with $(^{87}Sr/^{86}Sr)_i$ ratios of 0.70788–0.70833. Their $(^{143}Nd/^{144}Nd)_i$ ratios show considerable variation, with a range of 0.512078–0.512285, corresponding to $\varepsilon_{Nd}(t)$ values of −7.6 to −3.5. Initial $^{176}Hf/^{177}Hf$ ratios have a range of 0.282501–0.282638, corresponding to $\varepsilon_{Hf}(t)$ values of −6.8 to −1.9.

The Siling quartz diorites, granodiorites, and enclaves also show wide ranges of Sr-Nd isotopic compositions, with $(^{87}Sr/^{86}Sr)_i$ ratios of 0.70606–0.70878 and $(^{143}Nd/^{144}Nd)_i$ ratios of 0.512194–0.512287, corresponding to $\varepsilon_{Nd}(t)$ values of −5.3 to −3.5. The $(^{176}Hf/^{177}Hf)_i$ ratio of one granodiorite sample (SL46) is 0.282617, corresponding to an $\varepsilon_{Hf}(t)$ value of −2.7.

The least-evolved Siling alkali feldspar granite sample (SL28) has a $(^{87}Sr/^{86}Sr)_i$ ratio of 0.70560 with a relatively low $^{87}Rb/^{86}Sr$ ratio. The whole-rock $\varepsilon_{Nd}(t)$ values of the Siling alkali feldspar granites are relatively uniform, ranging from −3.2 to −2.5. The $(^{176}Hf/^{177}Hf)_i$ ratio of sample SL03 (from which the in situ zircon Hf isotopic composition was determined) is 0.282656, corresponding to an $\varepsilon_{Hf}(t)$ value of −1.3.

The whole-rock Sr-Nd-Hf isotopic compositions of the Siling gabbros are thus more enriched than those of the coexisting granites, highlighting the reversed isotope character of the complex (Figure 6).

5. Discussion

5.1. Ages of Rock Units in the Siling Complex

The Siling alkali feldspar granite has been previously dated at 89.8–93.4 Ma by the K-Ar method for biotite (Lu et al., 2008). According to our new LA-ICP-MS zircon U-Pb age data, the Siling alkali feldspar granite should form at ca. 129 Ma, consistent with recent dating results (131.0 ± 3.0 Ma; Wu et al., 2012). The 90–93 Ma biotite age is thus interpreted as recording a later thermal disturbance of the K-Ar isotopic system due to its low closure temperature (300°C–350°C; Harrison et al., 1979; Lee et al., 1997). The inferred granite crystallization age of ca. 130 Ma closely compares to that of other spatially associated granites (135–126 Ma; Figure 1a; Jiang et al., 2011; Li

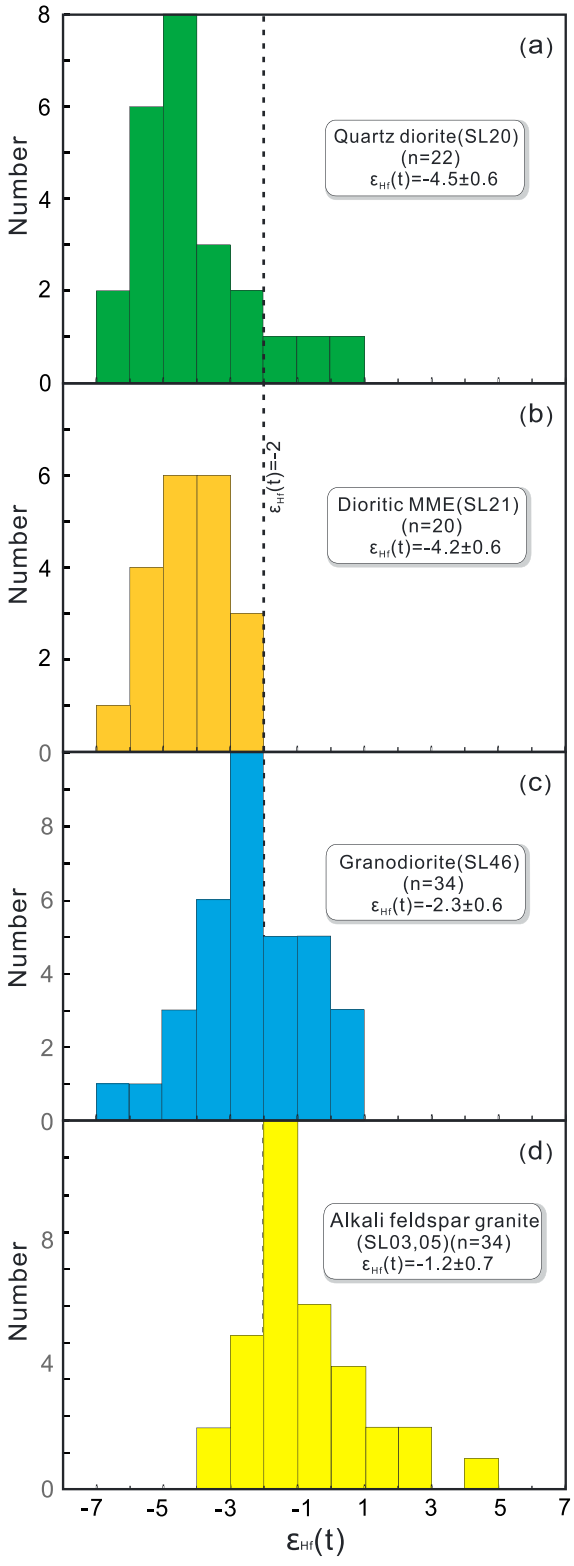

Figure 5. Histogram of $\varepsilon_{Hf}(t)$ values for zircons from the (a) Siling quartz diorite, (b) dioritic MME, (c) granodiorite, and (d) alkali feldspar granite. Zircons from the Siling quartz diorite and dioritic MME show more enriched Hf isotopic compositions than those from the granodiorite and alkali feldspar granite.

et al., 2013; Sun et al., 2015; Wong et al., 2009; Xia et al., 2016; Xiang et al., 2017; Yang et al., 2012; Zhou et al., 2013).

Zircon U-Pb ages of the quartz diorite and granodiorite (127–129 Ma) are indistinguishable from the alkali feldspar granite ages; that is, they are ~127–129 Ma, which is consistent with their field relations, including gradational contacts between the granitic units. Small-scale granite back-veins in the Siling massive gabbro (Figure 2a) further indicate that the Siling gabbro and alkali feldspar granite were emplaced contemporaneously (Barbarin, 2005), thereby highlighting the temporal relationships among rock units in the Siling complex.

5.2. Magma Mixing and the Origin of Quartz Diorite and Granodiorite

5.2.1. Genesis of the Enclaves

Enclaves hosted by the Siling granodiorite and alkali feldspar granite have fine-grained igneous textures (Figure 2e) and locally quenched margins. They yield a crystallization age similar to that of their host rocks (ca. 128 Ma; Figures 4a and 4b), thus precluding the possibility that they represent crustal xenoliths (cf. Maas et al., 1997; Xu et al., 2006) or restites (cf. Chappell & Wyborn, 2012; Vernon, 2007). Their distinct Sr-Nd-Hf isotopic compositions relative to their host rocks also preclude the possibility that they represent autoliths (cf. Donaire et al., 2005). Acicular apatite in the enclaves (Figure 2f) indicates relatively rapid crystallization (quenching). Felsic xenocrysts such as partially resorbed plagioclase and ocellar quartz (Figure 2d) are interpreted to have been mechanically captured by the enclave magma (Cheng et al., 2012; Plail et al., 2018; Ubide et al., 2014; Zhang et al., 2016), suggesting that the Siling enclaves were formed by the injection of relatively mafic magma into granitic melt. The injected mafic magma would have undergone rapid crystallization in the relatively cool felsic host melt.

5.2.2. Formation of Quartz Diorite and Granodiorite

Both the presence of dioritic MMEs and the uniform ages of all the units of the Siling complex are consistent with the quartz diorite and granodiorite having been formed by the mixing of gabbroic and granitic magmas. Evidence of such a hybrid origin includes the following. First, there is ample evidence of mineral-scale disequilibrium or significant core-rim mineral zoning, such as rapakivi K-feldspar, quartz mantled by K-feldspar (Figure 2c), quartz ocelli, sieve-textured plagioclase (Figure 3), and core-rim zoned zircons (Figure 4f; cf. Ma et al., 2017; Wang et al., 2008b; Xu et al., 1999; Zhang et al., 2016). Second, Sr-Nd-Hf isotopic signatures are intermediate between those of gabbro and alkali feldspar granite (Table 3; Figure 6). Third, the diorite and granodiorite show highly variable zircon Hf isotopic compositions ($\varepsilon_{Hf}(t)$ = −7.0 to +0.5 and −6.1 to +0.8, respectively; Tables S4 and 2 and Figures 5a and 5c; Gagnevin et al., 2011; Griffin et al., 2002; Shaw & Flood, 2009; Shaw et al., 2011; Stelten et al., 2013). Fourth, there is a sharp increase in plagioclase An contents from resorbed, sieve-textured sodic cores (~An_{32-46}, ~An_{33-38}) to normally zoned calcic rims (An_{29-64}, An_{17-54}; Figures 3a and 3b). Fifth, linear trends are observed in most whole-rock major- and trace-element contents (Figure S3; Plail et al., 2018). Mass-balance calculations (Figure 7) indicate that quartz diorite and granodiorite can be produced by the mixing of Siling gabbroic and granitic magmas in the approximate proportions of 55:45 to 88:12. Some mixing/mingling may have taken place in upper

Table 3
Sm-Nd and Rb-Sr Isotopic Compositions of the Gabbros, Quartz Diorites, MMEs, Granodiorites, and Alkali Feldspar Granites From the Siling Complex

Sample no.	SiO_2 wt.%	Sm (ppm)	Nd (ppm)	$^{147}Sm/^{144}Nd$	$^{143}Nd/^{144}Nd$	$(^{143}Nd/^{144}Nd)_i$	$\varepsilon_{Nd}(t)$	T_{DM2} (Ma)	Rb (ppm)	Sr (ppm)	$^{87}Rb/^{86}Sr$	$^{87}Sr/^{86}Sr$	$(^{87}Sr/^{86}Sr)_i$
The Siling gabbros													
SL39	45.33	5.07	21.0	0.1465	0.512323 ± 2	0.512201	−5.2	1319	75.8	544	0.41	0.70867 ± 4	0.70812
SL40	45.00	4.92	21.1	0.1414	0.512403 ± 10	0.512285	−3.5	1191	97.4	570	0.50	0.70888 ± 5	0.70796
SL41	46.68	4.05	18.1	0.1362	0.512330 ± 4	0.512217	−4.9	1307	81.1	611	0.39	0.70858 ± 4	0.70788
SL42	46.70	4.34	19.8	0.1334	0.512189 ± 3	0.512078	−7.6	1531	78.3	774	0.30	0.70887 ± 3	0.70833
SL43	45.60	4.49	19.8	0.1390	0.512257 ± 5	0.512141	−6.4	1423	79.8	633	0.37	0.70855 ± 5	0.70788
SL44	46.19	4.03	18.0	0.1362	0.512192 ± 3	0.512079	−7.6	1526	102	818	0.37	0.70889 ± 5	0.70822
SL45	45.15	4.74	20.1	0.1433	0.512367 ± 4	0.512248	−4.3	1249	84.7	737	0.34	0.70853 ± 4	0.70792
The Siling quartz diorites and granodiorites													
SL20	59.29	7.09	35.4	0.1216	0.512388 ± 3	0.512287	−3.5	1215	142	502	0.83	0.70862 ± 4	0.70712
SL23	63.44	7.74	39.6	0.1188	0.512305 ± 5	0.512207	−5.1	1346	142	350	1.19	0.71093 ± 5	0.70878
SL46	66.10	5.57	29.6	0.1143	0.512320 ± 5	0.512225	−4.7	1323	139	430	0.95	0.70850 ± 5	0.70678
SL26	67.20	4.93	27.0	0.1109	0.512287 ± 2	0.512194	−5.3	1376	117	448	0.76	0.70821 ± 3	0.70683
The Siling MMEs													
SL21	54.79	9.46	48.9	0.1175	0.512337 ± 3	0.512239	−4.4	1296	114	426	0.78	0.70944 ± 6	0.70802
SL15	60.86	13.2	53.3	0.1503	0.512324 ± 3	0.512199	−5.2	1317	337	188	5.25	0.71590 ± 4	0.70641
SL13	65.75	29.9	105	0.1723	0.512419 ± 5	0.512276	−3.7	1166	138	75.8	5.35	0.71571 ± 5	0.70606
The Siling alkali feldspar granites													
SL28	70.25	7.38	42.6	0.1053	0.512426 ± 3	0.512338	−2.5	1155	198	66.8	8.69	0.72129 ± 5	0.70560
SL02	74.91	9.18	43.7	0.1277	0.512412 ± 7	0.512304	−3.1	1178	379	22.0	50.4	—	—
SL03	73.64	10.6	51.0	0.1260	0.512408 ± 6	0.512302	−3.2	1184	297	43.3	20.1	—	—
SL04	75.84	8.40	41.8	0.1221	0.512432 ± 9	0.512329	−2.6	1145	392	14.4	79.7	—	—
SL05	76.61	7.50	31.5	0.1447	0.512432 ± 8	0.512310	−3.0	1146	410	12.5	96.1	—	—
SL06	76.10	8.75	35.9	0.1480	0.512449 ± 8	0.512324	−2.8	1119	473	12.4	112	—	—

crustal levels (as recorded by MMEs in granodiorite and alkali feldspar granite; cf. Cheng et al., 2012), but most should have taken place in deeper crustal reservoirs or during magma ascent, with the formation of quartz diorite and granodiorite magmas (cf. Jacob et al., 2015; Laumonier et al., 2014; Zhang et al., 2016).

Radiogenic isotopes attain equilibrium more quickly during mixing than do major and trace elements (Lesher, 1990; Poli et al., 1996), so the distinct isotopic compositions of the Siling MMEs preclude the possibility that mixing with the host magmas significantly shaped their composition (cf. Zhang et al., 2016). The similarity between zircon $\varepsilon_{Hf}(t)$ values of dioritic MMEs and quartz diorite (−4.5 ± 0.6 and −4.2 ± 0.6, respectively) further indicate that magma with a composition comparable with that of the quartz diorite contributed to the formation of the dioritic MMEs (Table 2; Figures 5a and 5b). The similar An contents of relict plagioclase cores in the quartz diorite (~$An_{32–46}$), the less-evolved granodiorite (~$An_{33–38}$), and the more-evolved granodiorite (SL26; ~$An_{32–42}$; Table S2; Figures 3a and 3b) suggest that the Siling hybrid granodioritic magma formed earlier than the dioritic magma. These observations indicate that mixing in the Siling complex was likely to have been a two-stage process as shown in Figure 8, with mixing first occurring between gabbro and granite magmas to form granodiorite magma and then between granodiorite and gabbro magmas to form the quartz diorite magma. The mixing origin of the Siling quartz diorite may provide insight into the formation of intermediate rocks elsewhere (cf. Dai et al., 2016; Laumonier et al., 2014; Price et al., 2016), especially those that are spatially and temporally related to mafic and felsic rocks (cf. Fodor & Johnson, 2016; Luo et al., 2015; Stelten et al., 2013; Zhang et al., 2016).

5.3. Origin of the Mafic End-Member

5.3.1. Role of Crustal Contamination

The Siling gabbros are characterized by low SiO_2 (45–47 wt.%) and moderately high MgO (6.0–6.7 wt.%) contents. However, they display "crust-like" trace-element and isotopic signatures, including enrichment in LILE (Rb, Ba, K) and Pb, depletion in Nb-Ta, low Ce/Pb (3–6) and Nb/U (9–15) ratios, high $(^{87}Sr/^{86}Sr)_i$ ratios (0.70788–0.70833), and low and variable $\varepsilon_{Nd}(t)$ (−7.6 to −3.5) and $\varepsilon_{Hf}(t)$ (−6.8 to −1.9) values, possibly reflecting high degrees of crustal contamination or assimilation.

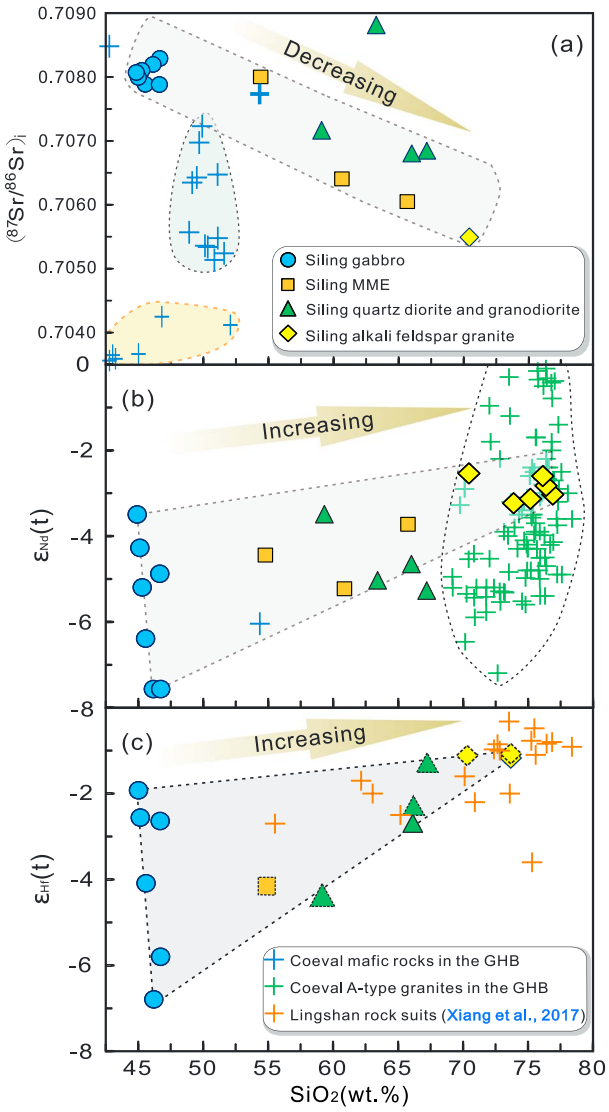

Figure 6. (a) SiO_2 versus $(^{87}Sr/^{86}Sr)_i$; (b) SiO_2 versus $\varepsilon_{Nd}(t)$; and (c) SiO_2 versus $\varepsilon_{Hf}(t)$ plots for the Siling gabbro, MME, quartz diorite, granodiorite, alkali feldspar granite, and spatially and temporally related mafic and granitic rocks. The rocks from the Siling complex show a broad inverse relationship between Sr–Nd–Hf isotopic compositions and SiO_2 content (i.e., the isotopically most depleted samples have the highest SiO_2 contents). Symbols rimmed by dashed and solid lines in Figure 6c represent in situ $\varepsilon_{Hf}(t)$ values for zircon and whole-rock $\varepsilon_{Hf}(t)$ values, respectively. Data sources for coeval mafic rocks (Table S6) and A-type granites are as in Figure 1.

Two possible crustal contamination scenarios are depicted in Figure 9, where depleted mantle-derived magmas are contaminated by different rocks with variable Sr-Nd-Nb compositions and Nb/U ratios. In both scenarios, exceptionally high degrees of contamination or assimilation (65–90 wt.%) would be required to account for the isotopic compositions, Nb/U ratios, and Nb contents of the Siling gabbro. Contamination by, or assimilation of, such large amounts of crust is thermally implausible (Glazner, 2007) and would have significantly modified the major- and trace-element compositions (other than Nb and U) of the gabbro, which is not observed. A lack of correlation between Sr-Nd-Hf isotopic ratios and Ce/Pb and Nb/U ratios for the Siling gabbro (not shown) also precludes significant crustal contamination. Further, the wide range of isotopic compositions of the Siling gabbro cannot be explained simply by variable silicate and/or carbonate crustal contamination, because the isotopically least enriched gabbro sample (SL40) has SiO_2, MgO, and CaO contents similar to those of the most enriched sample (SL42; Table S5).

Xia et al. (2017) proposed that the Hangzhou and surrounding areas (Figure 1a) where the Siling complex is exposed were in an intraoceanic arc zone during the Neoproterozoic amalgamation between the Yangtze and Cathaysia blocks, lacking pre-Neoproterozoic basement rocks. This would mean that basement rocks in the Siling area had been isotopically depleted until ~130 Ma when extensive magmatism commenced in the region (e.g., Li et al., 2009; Xia et al., 2017). The crust-like trace-element and isotope character of the Siling gabbro is thus chiefly ascribed to inheritance from its mantle source, although its heterogeneous Sr-Nd-Hf isotopic compositions suggest contributions from more than one source.

5.3.2. Nature of the Mafic Magma Sources

The Sr-Nd-Hf isotopic compositions of the Siling gabbro [$(^{87}Sr/^{86}Sr)_i$ = 0.70788–0.70833; $\varepsilon_{Nd}(t)$ = −7.6 to −3.5; $\varepsilon_{Hf}(t)$ = −6.8 to −1.9] are significantly more enriched than those of depleted mantle (DM) [$(^{87}Sr/^{86}Sr)_{128Ma}$ = 0.70258; ε_{Nd}(128 Ma) = +9.3; ε_{Hf}(128 Ma) = +15.9; Workman & Hart, 2005], thereby precluding its derivation solely from the partial melting of depleted mantle peridotite. The abundance of amphibole in the Siling gabbro (Figure 2e) attests to a high initial H_2O content in the mafic magma, with 4–6 wt.% H_2O at a crystallinity of up to 30 vol.% (Pichavant et al., 2002), further supporting this interpretation (H_2O_{MORB} < 0.5 wt.%; Kelley et al., 2006). Although crystal fractionation of anhydrous minerals may have elevated the H_2O content of the Siling gabbro, initial melts with high H_2O contents would be required. In addition, the available petrographical observations, significant LILE and LREE enrichment, and enriched Sr-Nd-Hf isotopic compositions require a volatile-rich, K_2O-rich, and isotopically enriched mantle source (cf. Guo et al., 2015; Lu et al., 2013; Ma et al., 2013; Yang et al., 2004).

Mafic shoshonitic igneous rocks such as the Siling gabbro (Figure S1a) are considered to be typically derived from partial melting of a metasomatized, enriched subcontinental lithospheric mantle (SCLM) (e.g., Guo et al., 2015; D. Liu et al., 2015; Lu et al., 2013). Volatile-bearing minerals such as phlogopite and/or amphibole are the major repositories for LILE in the lithospheric mantle (Foley et al., 1996; Ionov et al., 1997). Experimental studies have verified that reactions between partial melts or fluids derived from subducted eclogite-facies crustal rocks and surrounding mantle peridotite produce phlogopite- and/or amphibole-bearing pyroxenite (i.e., veined "metasomes"; Dasgupta et al., 2007; Herzberg, 2011; Herzberg et al., 2014; Kokfelt et al., 2006; Prelević et al., 2013; Sobolev et al., 2005, 2007). The high concentrations of LILE, LREE, and volatiles that characterize shoshonitic igneous suites are assumed to have been introduced into their mantle source in this way. Partial melting of such a "hybridized" mantle source generates shoshonitic

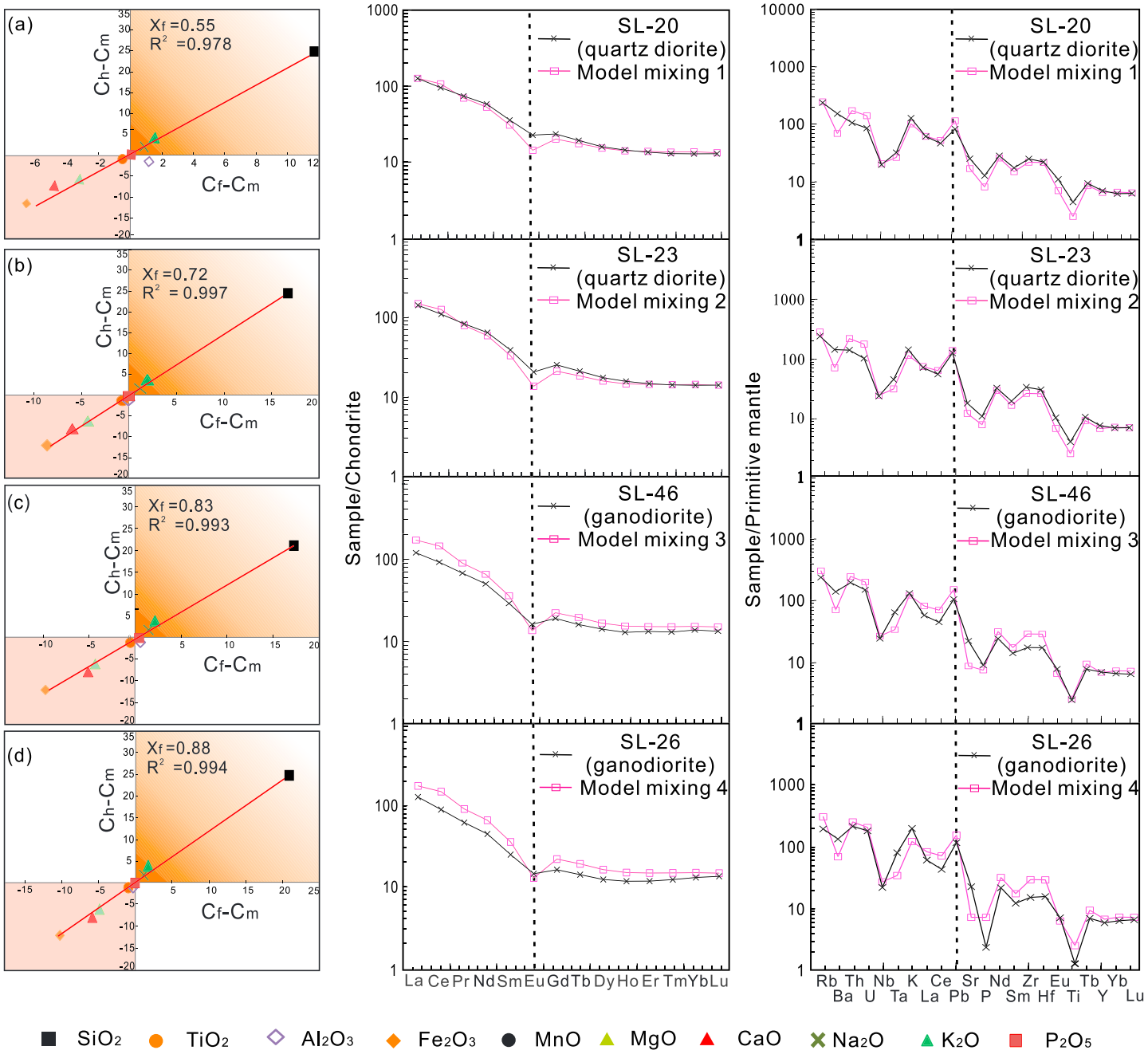

Figure 7. Whole-rock mixing test for major elements using mass-balance calculations of the type $C_h^i = C_f^i \times X_f + C_m^i \times (1 - X_f)$ (where C_h^i is the concentration of element *i* in the hybrid magma, C_m^i is the composition of the mafic end-member, C_f^i is the composition of the felsic end-member, and X_f is the mass fraction of the felsic end-member magma). The average composition of the Siling gabbro samples was used as the mafic end-member and the least-evolved composition of the Siling alkali feldspar granite sample (SL28) as the felsic end-member. The major-element compositions of the quartz diorite and granodiorite plot on a straight line that passes through the origin, indicating that they were formed by mixing of the modeled end-member magmas. The red line represents the theoretical straight line. Proportions of the felsic end-member in the rocks are 55%–88% for the quartz diorite and granodiorite. Some of the whole-rock scatter may have resulted from crystal-liquid fractionation of both end-member magmas and/or more complex mixing behavior (Zhang et al., 2016).

mafic magmas with relatively high K_2O, H_2O, and LILE contents and enriched Sr-Nd-Hf isotopic signatures relative to magmas derived from pure mantle peridotite (Herzberg, 2011; Sobolev et al., 2005, 2007). All these compositional characteristics apply to the Siling gabbro. Its significant depletions in Nb and Ta is, moreover, a characteristic fingerprint of subduction-zone magmatism (e.g., Duggen et al., 2005; Zeng et al., 2016), and its strong enrichment in Pb relative to Ce, and the resulting positive Pb anomalies and low

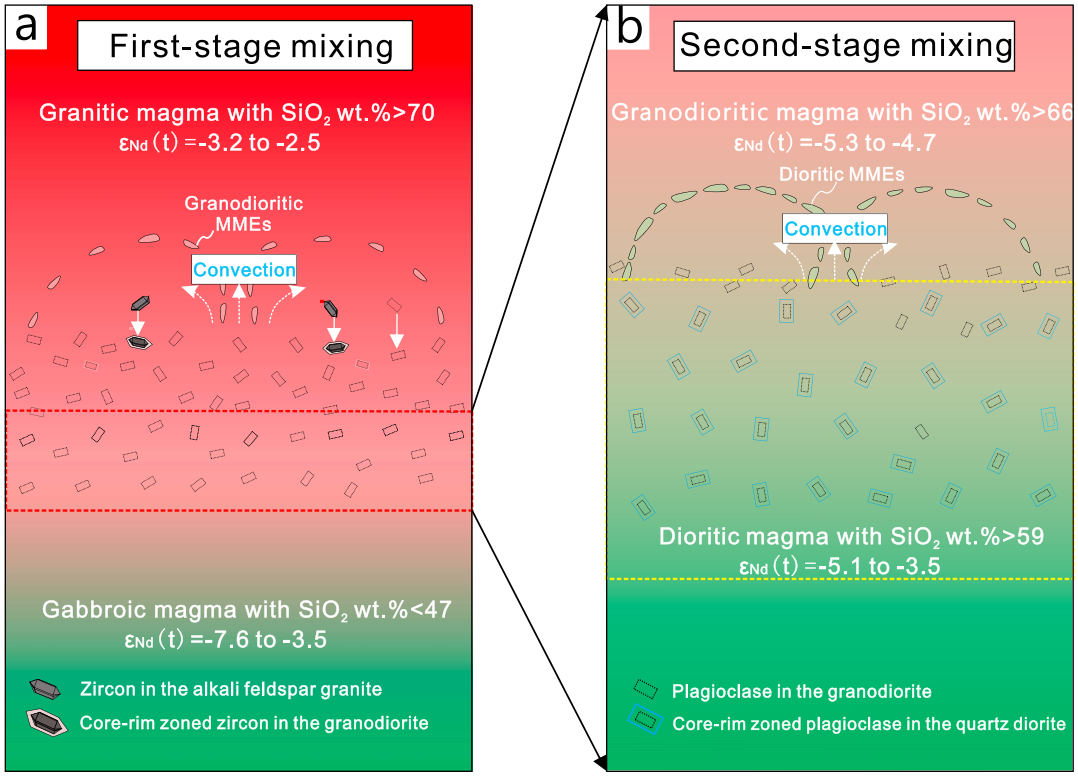

Figure 8. Schematic diagram showing the progressive, two-stage magma mixing process proposed for the formation of the Siling quartz diorite and granodiorite. (a) At an early stage of the magmatism, the underplating gabbro magma mixed with juvenile lower crust derived granite magma to produce granodiorite magma with zircons that show core-rim zoning. At this stage, a small amount of hybrid granodiorite magma was injected into the granite magma due to convection, forming the granodioritic MMEs. (b) The resulting granodiorite magma that was located at the contact boundary was mixed with gabbro magma to form the quartz diorite magma with sieve-textured, core-rim zoned plagioclase. Many dioritic MMEs enclosed in the granodiorite were also formed due to the injection of a large amount of dioritic magma.

Ce/Pb ratios (3–6), likely reflects the contribution of pelagic sediment in its source (Plank, 2014). It is therefore concluded that the mafic magma parent of the Siling gabbro was formed through partial melting of a pyroxenite-bearing enriched SCLM that was previously modified by Neoproterozoic subduction-related metasomatism (e.g., Wang et al., 2015).

As discussed above, isotopic variations in the Siling gabbro cannot be explained by crustal contamination or assimilation and most likely reflect mantle-inherited heterogeneity. Mantle heterogeneity, even on a meter-scale, has long been invoked to explain isotopic diversity between and within igneous suites (Borghini et al., 2013; Herzberg, 2011; Herzberg et al., 2014; Hofmann, 2003; Sobolev et al., 2005, 2007; Zeng et al., 2017), due to partial melting of pyroxenite-rich to depleted peridotite mantle sources (e.g., Kokfelt et al., 2006; Shorttle et al., 2014; Stracke & Bourdon, 2009; Zhang et al., 2012). The Siling gabbro displays decreasing Th/Nb and increasing Nb/Nb* ratios with increasing $\varepsilon_{Nd}(t)$ values (Figures 10a and 10b). Similar correlations have been observed for Icelandic basalts (Kokfelt et al., 2006; Stracke & Bourdon, 2009) and East Pacific Rise basalts (Zhang et al., 2012), which are considered to record partial melting of a heterogeneous mantle source (Kokfelt et al., 2006; Stracke & Bourdon, 2009; Zhang et al., 2012).

High Th/Nb and low Nb/Nb* ratios are typical signatures of continental crust (Rudnick & Gao, 2003), and variations in Sr-Nd-Hf isotopic compositions reflect distinct source components. The progression to less continental crust-like Th/Nb and Nb/Nb* ratios along with more depleted Nd isotopic signatures (Figures 10a and 10b) suggests that the contribution of enriched components decreased systematically. Additionally, the isotopically less enriched gabbro evolved with lower Sm/Yb ratios (Figure 10c), implying partial melting of distinct sources at different mantle levels (e.g., Zhang et al., 2012). Due to the more fusible nature and lower solidus, for an upwelling hybridized mantle composed of pyroxenite and peridotite, melting would

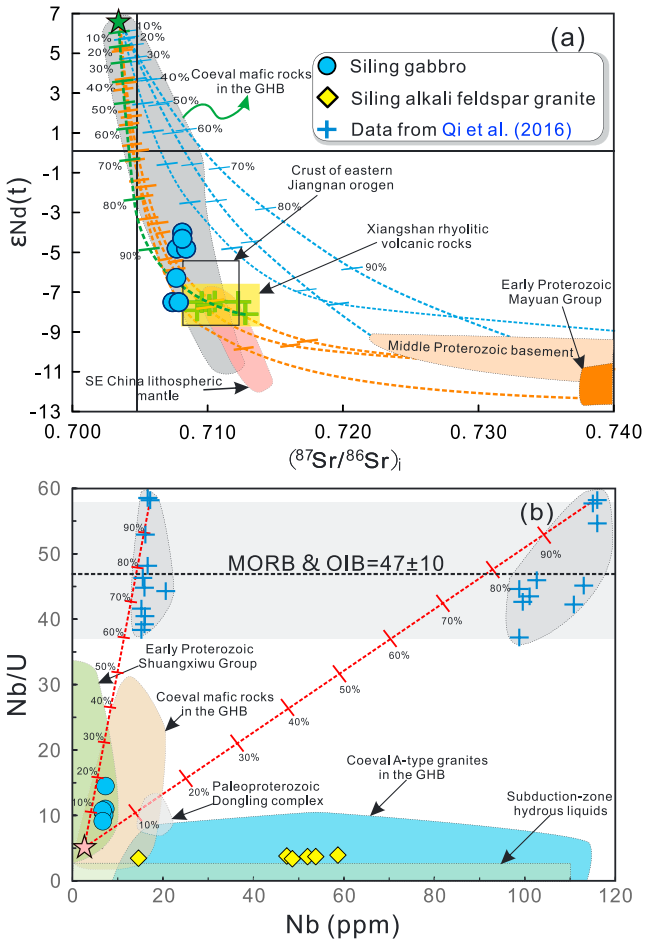

Figure 9. (a) $\varepsilon_{Nd}(t)$ versus $(^{87}Sr/^{86}Sr)_i$ ratio diagram and (b) Nb/U versus Nb diagram for assessing the role of crustal contamination in the formation of the Siling gabbro. The compositions of end-members or components assumed for contamination calculations are as follows: (1) the average composition of the Longyou ultramafic samples HTSM 2, 5, 7, and 8 is used to represent DM-derived melts and shown by the green star in Figure 9a: $(^{87}Sr/^{86}Sr)_i$ = 0.70354–0.70360; ε_{Nd}(128 Ma) = +5.9 to +6.6; Sr = 1,140–1,210 ppm; Nd = 48.4–52.9 ppm (Qi et al., 2016). (2) The Early Proterozoic basement (granulite and schist; Yuan et al., 1991), the Middle Proterozoic basement (schist; Hu, 1998), the Xiangshan rhyolitic volcanic rock (sample X9–21; porphyritic lava; Jiang et al., 2005), the Shuangxiwu group (Li et al., 2009), and the Paleoproterozoic Dongling complex (Chen & Xing, 2016) are assumed to be represented contaminants. (3) For the Quzhou mafic (samples HBM3) and Longyou (samples HTSM7) ultramafic intrusions in Figure 9b, Nb = 16.4–116 ppm and Nb/U = 58.3–58.6. (4) The Early Proterozoic Shuangxiwu sample 04ZJ67 with the lowest Nb content (2.58 ppm) and Nb/U ratio (5.0; Li et al., 2009) is expressed by the pink star in Figure 9b. The composition of the southeastern China lithospheric mantle is assumed to be represented by the Tieshan and Yangfang syenites (Wang et al., 2005). Compositions of subduction-zone hydrous melts are from Kessel et al. (2005). Data sources for coeval mafic rocks (Table S6) and A-type granites are as in Figure 1.

commence with the deeper pyroxenite (Lambart et al., 2009). The observed correlations between trace-element and isotopic compositions therefore indicate that the mafic magma parent of the Siling gabbro represents a variable mixture of magmas derived from diverse mantle sources, melting at different levels. Nevertheless, simple binary mixing models indicate that pyroxenite-derived melt may contribute up to 85 wt.% of the magma (Figure 10d). Sr isotopes diffuse more quickly and more efficiently than Nd-Hf isotopes during mixing (Lesher, 1990; Menzies & Murthy, 1980), so the latter tend to better record mantle source heterogeneity, which is consistent with their greater variability than that of Sr isotopes in the Siling gabbro (Table 3; Figure 6). The Siling gabbro thus reveals the existence of an enriched SCLM during the Mesozoic in south China (e.g., Wang et al., 2005), at least beneath the GHB.

5.4. Origin of the Felsic End-Member

5.4.1. A-Type Affinity

The Siling alkali feldspar granite is classified as a typical aluminous A-type granite because of its (1) high whole-rock 10,000 × Ga/Al ratios and Zr + Nb + Ce + Y concentrations (Whalen et al., 1987; Figure 11); (2) high zircon saturation temperatures (T_{Zr} = 773–799°C; Boehnke et al., 2013) (King et al., 2001); (3) high total alkali and HFSE concentrations (Frost et al., 2001); and (4) ferroan whole-rock composition (Table S5) and Fe- and F-rich biotite (Table S1; Frost & Frost, 2010). The petrogenesis of A-type granite is still debated (e.g., Barker et al., 2013; Huang et al., 2011; Namur et al., 2011; Papoutsa et al., 2016; Xu & Tang, 2017; Yang et al., 2017), but it is generally accepted that it represents high-temperature magma that crystallized at relatively low melt-H_2O concentrations (Bonin, 2007; Creaser et al., 1991; Collins et al., 1982; Frost et al., 2001; Frost & Frost, 2010; King et al., 1997, 2001).

5.4.2. Genesis of the Alkali Feldspar Granite

The Siling alkali feldspar granite exhibits Nd-Hf isotopic compositions ($\varepsilon_{Nd}(t)$ = −3.2 to −2.5; $\varepsilon_{Hf}(t)_{whole\text{-}rock}$ = −1.3) closely approaching those of the isotopically least enriched Siling gabbro sample in the present study (sample SL40; $\varepsilon_{Nd}(t)$ = −3.5; $\varepsilon_{Hf}(t)_{whole\text{-}rock}$ = −1.9), suggesting that the two rock types are petrogenetically related. The Siling A-type granite may thus have formed through extreme fractional crystallization from the isotopically least enriched gabbroic magma (cf. Mushkin et al., 2003; Namur et al., 2011; Zhong et al., 2011), or partial melting of juvenile lower crust rocks with isotopic compositions similar to those of the exposed Siling gabbro (represented by sample SL40; cf. Ratajeski et al., 2001; Ratajeski et al., 2005; Tang et al., 2014; Wenner & Coleman, 2004).

However, anhydrous granite cannot be derived by fractional crystallization from such hydrous mafic magma (sample SL40, 4–6 wt.% H_2O; Pichavant et al., 2002). Granitic magma derived by fractional crystallization from such a mafic parent would have higher or equivalent H_2O concentrations (Annen et al., 2006; Claeson & Meurer, 2004). In contrast, the A-type affinity of the Siling granitic magma indicates that it had a low H_2O content (cf. Bonin, 2007; Frost et al., 2001; Frost & Frost, 2010; King et al., 1997; Whalen et al., 1987). The absence of large volumes of mafic cumulates in the Siling area is also consistent with the interpretation that Siling-type mafic magma was not the parental magma for fractional crystallization of the Siling alkali feldspar granite.

The following model of granite genesis is therefore proposed. The Siling alkali feldspar granite parental magma was produced by partial melting of juvenile mafic lower crust that is isotopically comparable with

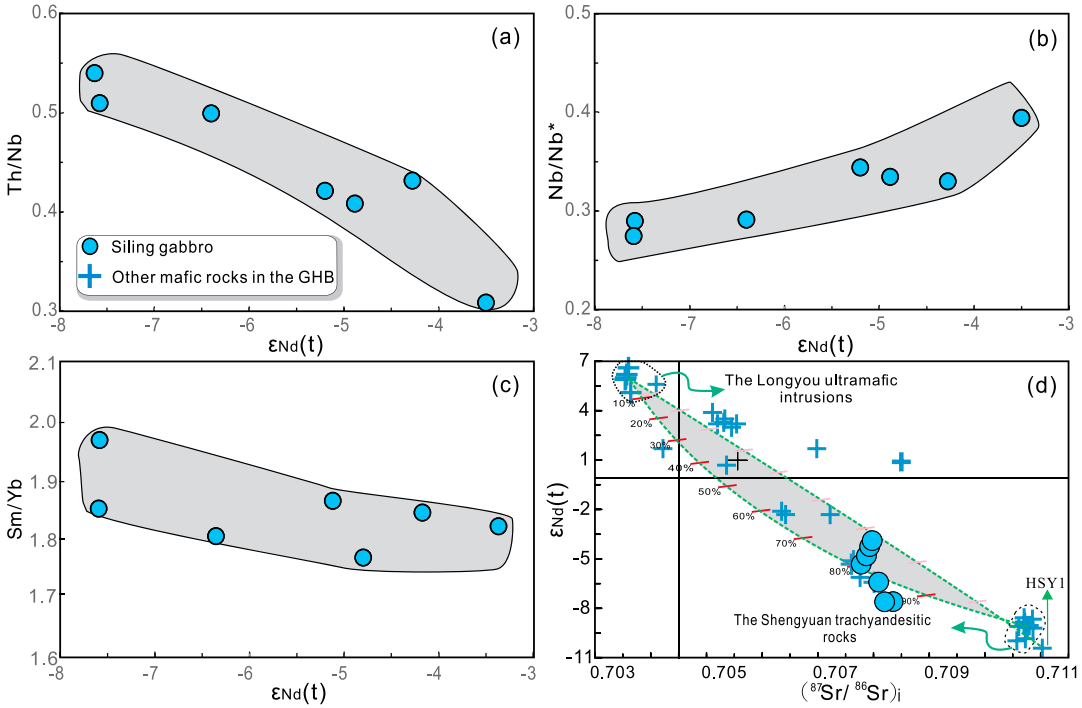

Figure 10. Correlations of $\varepsilon_{Nd}(t)$ values with (a) Th/Nb, (b) Nb/Nb*, and (c) Sm/Yb ratios. (d) $\varepsilon_{Nd}(t)$ versus $(^{87}Sr/^{86}Sr)_i$ diagram for the Siling gabbro. The average Sr and Nd isotopic compositions of the Longyou ultramafic intrusions (Qi et al., 2016) are used to represent the isotopic compositions of the asthenosphere mantle-derived melts. The enriched end-members are represented respectively by the average compositions of the Shengyuan trachyandesitic rocks (Shu et al., 2017) and the isotopically most enriched mafic dyke sample HSY1 from the GHB (Qi et al., 2012). Data sources for coeval mafic rocks (Table S6) are as in Figure 1.

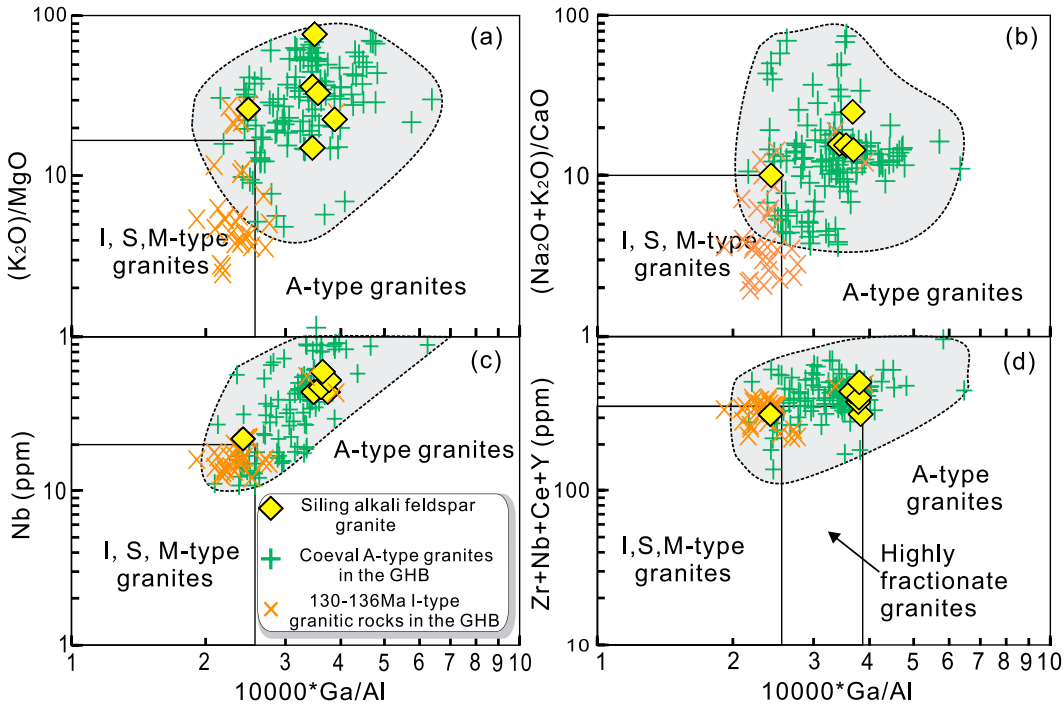

Figure 11. (a) (K2O/MgO), (b) (Na2O + K2O)/CaO, (c) Nb, and (d) (Zr + Nb + Ce + Y) versus 10,000 × Ga/Al discrimination diagrams (after Whalen et al., 1987), showing A-type affinity of the Siling alkali feldspar granite. Data sources for coeval A-type granites as in Figure 1. Data for I-type granitic rocks in the area that predate the ~129 Ma A-type granites are from L. Zhao et al. (2016) and Zhou (2016).

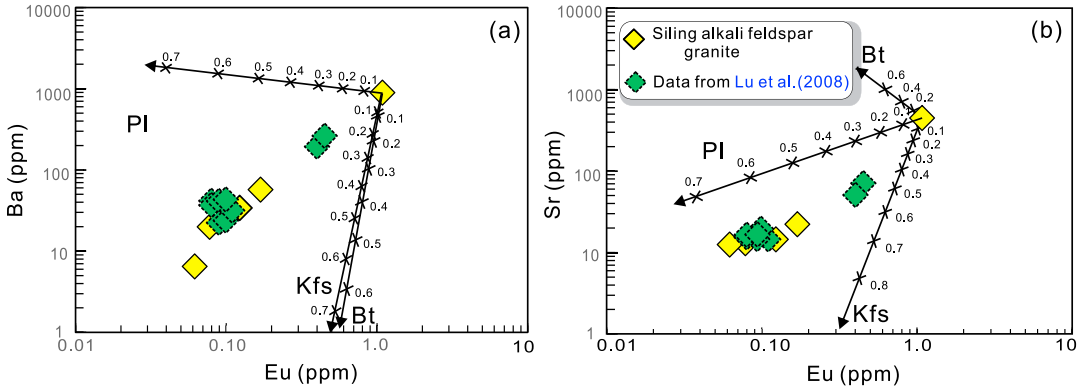

Figure 12. Eu versus (a) Ba and (b) Sr diagrams, showing that fractional crystallization of plagioclase and K-feldspar played an important role in the generation of the Siling alkali feldspar granite. Partition coefficients of Eu, Ba, and Sr are from Stix and Gorton (1990), Mahood and Hildreth (1983), and Ewart and Griffin (1994) for plagioclase, K-feldspar, and biotite.

the least enriched gabbro sample (SL40). At an early stage of magmatism, most of the mantle-derived magma was emplaced in the deep crust, forming juvenile lower crust. Continued injection of mantle-derived magmas led to partial melting of crystallized juvenile lower crust to produce slightly earlier I-type granitic melt, such as the Tianmushan basin volcanic rocks (136–130 Ma; L. Zhao et al., 2016) and the Xianxia and Tonglizhuang granites (131–132 Ma; Wu et al., 2012; Zhou, 2016; Figure 11), after incubation for tens to hundreds of kiloyears of magmatism in the area (Annen et al., 2006; Blundy & Annen, 2016). Then the dehydrated granulitic restite source after extraction of I-type granitic melts further melted under higher temperatures to produce relatively anhydrous, high-temperature, and F-rich granitic melt (Collins et al., 1982; Huang et al., 2011; King et al., 2001; Landenberger & Collins, 1996; Whalen et al., 1987; J. L. Zhao et al., 2016). The resulting A-type granitic melt ascended to the exposed upper crust where the Siling alkali feldspar granite was formed, coupled with the fractional crystallization of plagioclase and K-feldspar (Figure 12). This view is in accordance with the lack of inherited zircons in the Siling alkali feldspar granite. Its high-temperature, F-rich character (indicated by the presence of fluorite aggregates, Figure 2b, and F-rich biotites, Table S1) may have lowered the magma viscosity sufficiently for efficient mixing with coexisting gabbroic magma (Annen et al., 2006; González-García et al., 2017).

6. Implications

Magma mixing commonly takes place between isotopically depleted mafic and enriched felsic magmas. Almost all mafic-felsic magma mixing models thus assume a more depleted composition for the mafic end-member in thoroughly mixed magmatic systems (e.g., Barbarin, 2005; Fodor & Johnson, 2016; Laumonier et al., 2014; Luo et al., 2015; Schleicher et al., 2016; Słaby & Martin, 2008; Ubide et al., 2014). However, as shown here for the Siling complex and in other studies (e.g., Coleman et al., 1992; Ratajeski et al., 2001; Waight et al., 2007; Xiang et al., 2017; Zhong et al., 2011; Table 1), reversed isotope magma mixing may also occur. The important implication of this type of magma mixing is that it may account not only for whole-rock but also for mineral-scale compositional trends that may at first sight require complex assimilation-fractional-crystallization (AFC) processes (e.g., the direct addition of enriched mantle-derived magmas versus magma recharge, combined with crustal assimilation).

For example, plagioclase phenocrysts with high-An content, high-$(^{87}Sr/^{86}Sr)_i$ zones and low-An content, low-$(^{87}Sr/^{86}Sr)_i$ zones, that is, crystals that record reversed isotope zoning (also referred to as decoupling between isotopic and chemical variations; Ginibre and Davidson, 2014), are characteristic of many phenocrysts erupted at arc volcanoes and crystals present in intrusive igneous rocks. Examples of this include andesite at Merapi (Chadwick et al., 2007), dacite at Capraia Volcano (Gagnevin et al., 2007), trachyandesite at El Chichón (Andrews et al., 2008; Davidson et al., 2001; Tepley et al., 2000), dacite at Parinacota (Ginibre & Davidson, 2014), anorthosite in the Bushveld Complex (Yang et al., 2013), and hawaiite at Skye Volcano (Font et al., 2008). The zonation in plagioclase is commonly assumed to record crustal assimilation (e.g., Borisova et al., 2013; Chadwick et al., 2007; Deegan et al., 2010), but reversed isotope magma mixing may

serve as an alternative explanation, which should at least be considered along with AFC models. High-An content, high-$(^{87}Sr/^{86}Sr)_i$ zones in plagioclase phenocrysts may represent zones that have crystallized from isotopically enriched mafic magma, whereas low-An content, low-$(^{87}Sr/^{86}Sr)_i$ zones may record the injection of isotopically relatively depleted, less-mafic melt. Mixing of compositionally contrasting magmas has been indeed identified in all volcanic magma systems in which plagioclase exhibits prominent reversed isotope zoning, including Merapi (Costa et al., 2013; Erdmann et al., 2016), Capraia Volcano (Gagnevin et al., 2011), El Chichón (Andrews et al., 2008; Tepley et al., 2000), Parinacota (Ginibre & Wörner, 2007), the Bushveld complex (Naldrett et al., 2009; Roelofse & Ashwal, 2012; Yang et al., 2013), and Skye Volcano (Font et al., 2008). Reversed isotope magma mixing may thus be more common than typically invoked. Caution is therefore warranted when a more depleted composition is presumed for the mafic end-member in mixing models, when isotopic equilibrium has already been established in MME-granitoid associations. Both normal and reversed isotope magma mixing should be considered in rigorous interpretations of thoroughly mixed magma systems.

In addition to better understand magmatic processes, reversed isotope signatures may also have implications for the growth of continental crustal. The crustal growth is a matter of ongoing debate (e.g., Gazel et al., 2015; Hawkesworth & Kemp, 2006), and detrital zircon U-Pb and Lu-Hf isotopic systematics have proven to be helpful in improving our understanding of this topic (e.g., Hawkesworth & Kemp, 2006; Iizuka et al., 2010; Liu et al., 2017; Xu et al., 2007). Most of the conclusions reached using this approach are predicated on the assumptions that high $\varepsilon_{Nd}(t)$ or $\varepsilon_{Hf}(t)$ values imply a continental growth event with mantle-derived magma added to continental crust, while low values imply the reworking of preexisting older crustal material (e.g., Belousova et al., 2010; Liu et al., 2017; Yang et al., 2009). However, reversed isotope signatures reflect the opposite, with isotopically enriched magma contributing to the growth of continental crust, while relatively depleted melts reflect reworking of juvenile crust. It is therefore suggested that the vertical growth of continental crust through the input of isotopically enriched magma should be considered further, particularly concerning reversed isotope signatures.

7. Conclusions

1. The Cretaceous Siling complex located in the GHB (south China) is composed of gabbro, quartz diorite, granodiorite, and alkali feldspar granite, with many MMEs enclosed in granodiorite and alkali feldspar granite. Field observations and zircon U-Pb age data indicate that all of the rock units crystallized contemporaneously at ca. 127–129 Ma.
2. The Siling quartz diorite and granodiorite crystallized from hybrid magmas of coexisting isotopically enriched gabbroic and relatively depleted granitic magmas, thus recording reversed isotope magma mixing. This highlights that the injection of mantle-derived mafic magma does not necessarily imprint comparatively depleted isotopic signature on the host felsic melt.
3. The Siling gabbro, characterized by variable yet enriched Sr-Nd-Hf isotopic composition, represents mixtures of magmas derived from diverse mantle sources melting at different levels. The Siling alkali feldspar granite with typical A-type affinities and relatively depleted isotopic signatures was derived from the remelting of juvenile lower crust.

Acknowledgments

The data presented in this paper are available from the corresponding author (xsxu@nju.edu.cn). We are sincerely grateful to Zhenyu He, Lei Liu, Wentao Hong, Kai Zhao, Xisong Zhang and Shijing Hang for the field investigations and helpful discussions. The thoughtful and constructive comments by Editor Michael Walter and two anonymous reviewers are greatly appreciated. This work was financially supported by the National Natural Science Foundation of China (grant 41430208) and the National Key R&D Program of China (grant 2016YFC0600203).

References

Andrews, B. J., Gardner, J. E., & Housh, T. B. (2008). Repeated recharge, assimilation, and hybridization in magmas erupted from El Chichón as recorded by plagioclase and amphibole phenocrysts. *Journal of Volcanology and Geothermal Research*, *175*, 415–426. https://doi.org/10.1016/j.jvolgeores.2008.02.017

Annen, C., Blundy, J. D., & Sparks, R. S. J. (2006). The genesis of intermediate and silicic magmas in deep crustal hot zones. *Journal of Petrology*, *47*, 505–539. https://doi.org/10.1093/petrology/egi084

Appleby, S. K., Graham, C. M., Gillespie, M. R., Hinton, R. W., & Oliver, G. J. H. (2008). A cryptic record of magma mixing in diorites revealed by high-precision SIMS oxygen isotope analysis of zircons. *Earth and Planetary Science Letters*, *269*, 105–117. https://doi.org/10.1016/j.epsl.2008.02.006

Barbarin, B. (2005). Mafic enclaves and mafic rocks associated with some granitoids of the central Sierra Nevada batholith, California: Nature and origin, and relations with the hosts. *Lithos*, *80*, 155–177. https://doi.org/10.1016/j.lithos.2004.05.010

Barker, F., Creaser, R. A., Price, R. C., & Wormald, R. J. (2013). Comment and reply on "A-type granites revisited: Assessment of a residual-source model". *Geology*, *19*(2), 163.

Belousova, E. A., Kostitsyn, Y. A., Griffin, W. L., Begg, G. C., O'Reilly, S. Y., & Pearson, N. J. (2010). The growth of the continental crust: constraints from zircon Hf-isotope data. *Lithos*, *119*(3–4), 457–466.

Black, L. P., & Gulson, B. L. (1978). The age of the Mud Tank carbonatite, Strangways Range, Northern Territory. *Journal of Australian Geology and Geophysics*, *3*(3), 227–232.

Blundy, J. D., & Annen, C. J. (2016). Crustal magmatic systems from the perspective of heat transfer. *Elements*, *12*(2), 115–120. https://doi.org/10.2113/gselements.12.2.115

Boehnke, P., Watson, E. B., Trail, D., Harrison, T. M., & Schmitt, A. K. (2013). Zircon saturation re-revisited. *Chemical Geology*, *351*, 324–334. https://doi.org/10.1016/j.chemgeo.2013.05.028

Bonin, B. (2007). A-type granites and related rocks: Evolution of a concept, problems and prospects. *Lithos*, *97*, 1–29. https://doi.org/10.1016/j.lithos.2006.12.007

Borghini, G., Rampone, E., Zanetti, A., Class, C., Cipriani, A., Hofmann, A. W., & Goldstein, S. L. (2013). Meter-scale Nd isotopic heterogeneity in pyroxenite-bearing Ligurian peridotites encompasses global-scale upper mantle variability. *Geology*, *41*(10), 1055–1058. https://doi.org/10.1130/G34438.1

Borisova, A. Y., Martel, C., Gouy, S., Pratomo, I., Sumarti, S., Toutain, J. P., … Métaxian, J. P. (2013). Highly explosive 2010 Merapi eruption: Evidence for shallow-level crustal assimilation and hybrid fluid. *Journal of Volcanology and Geothermal Research*, *261*, 193–208. https://doi.org/10.1016/j.jvolgeores.2012.11.002

Bouvier, A., Vervoort, J. D., & Patchett, P. J. (2008). The Lu−Hf and Sm−Nd isotopic composition of Chur: Constraints from unequilibrated chondrites and implications for the bulk composition of terrestrial planets. *Earth and Planetary Science Letters*, *273*, 48–57. https://doi.org/10.1016/j.epsl.2008.06.010

Chadwick, J. P., Troll, V. R., Ginibre, C., Morgan, D., Gertisser, R., Waight, T. E., & Davidson, J. P. (2007). Carbonate assimilation at Merapi Volcano, Java, Indonesia: Insights from crystal isotope stratigraphy. *Journal of Petrology*, *48*, 1793–1812. https://doi.org/10.1093/petrology/egm038

Chappell, B. W., & Wyborn, D. (2012). Origin of enclaves in S-type granites of the Lachlan Fold Belt. *Lithos*, *154*, 235–247. https://doi.org/10.1016/j.lithos.2012.07.012

Chen, Z. H., & Xing, G. F. (2016). Geochemical and zircon U−Pb−Hf−O isotopic evidence for a coherent Paleoproterozoic basement beneath the Yangtze Block, south China. *Precambrian Research*, *279*, 81–90. https://doi.org/10.1016/j.precamres.2016.04.002

Cheng, Y., Spandler, C., Mao, J., & Rusk, B. G. (2012). Granite, diabase and mafic microgranitoid enclaves in the Gejiu area, Yunnan Province, China: A case of two-stage mixing of crust- and mantle-derived magmas. *Contributions to Mineralogy and Petrology*, *164*, 659–676. https://doi.org/10.1007/s00410-012-0766-0

Chu, M. F., Chung, S. L., Song, B., Liu, D., O'Reilly, S. Y., Pearson, N. J., & Wen, D. J. (2006). Zircon U−Pb and Hf isotope constraints on the Mesozoic tectonics and crustal evolution of southern Tibet. *Geology*, *34*(9), 745–748. https://doi.org/10.1130/G22725.1

Chung, S. L., Chu, M. F., Ji, J., O'Reilly, S. Y., Pearson, N. J., Liu, D., & Lo, C. H. (2009). The nature and timing of crustal thickening in southern Tibet: Geochemical and zircon Hf isotopic constraints from postcollisional adakites. *Tectonophysics*, *477*(1-2), 36–48. https://doi.org/10.1016/j.tecto.2009.08.008

Claeson, D. T., & Meurer, W. P. (2004). Fractional crystallization of hydrous basaltic "arc-type" magmas and the formation of amphibole-bearing gabbroic cumulates. *Contributions to Mineralogy and Petrology*, *147*, 288–304. https://doi.org/10.1007/s00410-003-0536-0

Clemens, J. D., & Stevens, G. (2016). Melt segregation and magma interactions during crustal melting: Breaking out of the matrix. *Earth-Science Reviews*, *160*, 333–349. https://doi.org/10.1016/j.earscirev.2016.07.012

Coleman, D. S., Frost, T. P., & Glazner, A. F. (1992). Evidence from the lamarck granodiorite for rapid Late Cretaceous crust formation in California. *Science*, *258*(5090), 1924–1926. https://doi.org/10.1126/science.258.5090.1924

Collins, W. J., Beams, S. D., White, A. J. R., & Chappell, B. W. (1982). Nature and origin of A-type granites with particular reference to southeastern Australia. *Contributions to Mineralogy and Petrology*, *80*(2), 189–200. https://doi.org/10.1007/BF00374895

Costa, F., Andreastuti, S., de Maisonneuve, C. B., & Pallister, J. S. (2013). Petrological insights into the storage conditions, and magmatic processes that yielded the centennial 2010 Merapi explosive eruption. *Journal of Volcanology and Geothermal Research*, *261*, 209–235. https://doi.org/10.1016/j.jvolgeores.2012.12.025

Creaser, R. A., Price, R. C., & Wormald, R. J. (1991). A-type granites revisited: Assessment of a residual-source model. *Geology*, *19*(2), 163–166. https://doi.org/10.1130/0091-7613(1991)019%3C0163:ATGRAO%3E2.3.CO;2

Dai, F. Q., Zhao, Z. F., Dai, L. Q., & Zheng, Y. F. (2016). Slab-mantle interaction in the petrogenesis of andesitic magmas: Geochemical evidence from postcollisional intermediate volcanic rocks in the Dabie Orogen, China. *Journal of Petrology*, *57*(6), 1109–1134. https://doi.org/10.1093/petrology/egw034

Dasgupta, R., Hirschmann, M. M., & Smith, N. D. (2007). Partial melting experiments of peridotite+CO_2 at 3 GPa and genesis of alkalic ocean island basalts. *Journal of Petrology*, *48*, 2093–2124. https://doi.org/10.1093/petrology/egm053

Davidson, J., Tepley, F., Palacz, Z., & Meffan-Main, S. (2001). Magma recharge, contamination and residence times revealed by in situ laser ablation isotopic analysis of feldspar in volcanic rocks. *Earth and Planetary Science Letters*, *184*(2), 427–442. https://doi.org/10.1016/S0012-821X(00)00333-2

Deegan, F. M., Troll, V. R., Freda, C., Misiti, V., Chadwick, J. P., McLeod, C. L., & Davidson, J. P. (2010). Magma-carbonate interaction processes and associated CO_2 release at Merapi Volcano, Indonesia: Insights from experimental petrology. *Journal of Petrology*, *51*, 1027–1051. https://doi.org/10.1093/petrology/egq010

Donaire, T., Pascual, E., Pin, C., & Duthou, J. L. (2005). Microgranular enclaves as evidence of rapid cooling in granitoid rocks: The case of the Los Pedroches granodiorite, Iberian Massif, Spain. *Contributions to Mineralogy and Petrology*, *149*, 247–265. https://doi.org/10.1007/s00410-005-0652-0

Duggen, S., Hoernle, K., Bogaard, P., & Garbe-Schonberg, D. (2005). Post-collisional transition from subduction- to intraplate-type magmatism in the westernmost Mediterranean: Evidence for continental-edge delamination of subcontinental lithosphere. *Journal of Petrology*, *46*, 1155–1201. https://doi.org/10.1093/petrology/egi013

Eisele, J., Sharma, M., Galer, S. J., Blichert-Toft, J., Devey, C. W., & Hofmann, A. W. (2002). The role of sediment recycling in EM-1 inferred from Os, Pb, Hf, Nd, Sr isotope and trace element systematics of the Pitcairn hotspot. *Earth and Planetary Science Letters*, *196*(3-4), 197–212. https://doi.org/10.1016/S0012-821X(01)00601-X

Erdmann, S., Martel, C., Pichavant, M., Bourdier, J. L., Champallier, R., Komorowski, J. C., & Cholik, N. (2016). Constraints from phase equilibrium experiments on pre-eruptive storage conditions in mixed magma systems: A case study on crystal-rich basaltic Andesites from mount Merapi, Indonesia. *Journal of Petrology*, *57*(3), 535–560. https://doi.org/10.1093/petrology/egw019

Ewart, A., & Griffin, W. L. (1994). Application of proton-microprobe data to trace-element partitioning in volcanic-rocks. *Chemical Geology*, *117*(1-4), 251–284. https://doi.org/10.1016/0009-2541(94)90131-7

Fodor, R. V., & Johnson, K. G. (2016). Origin of Miocene andesite and dacite in the Goldfield-Superstition volcanic province, central Arizona: Hybrids of mafic and silicic magma mixing. *Geochimica et Cosmochimica Acta*, *185*, 394–417. https://doi.org/10.1016/j.gca.2016.04.001

Foley, S., Venturelli, G., Green, D. H., & Toscani, L. (1987). The ultrapotassic rocks: Characteristics, classification, and constraints for petrogenetic models. *Earth-Science Reviews*, *24*(2), 81–134. https://doi.org/10.1016/0012-8252(87)90001-8

Foley, S. F., Jackson, S. E., Fryer, B. J., Greenouch, J. D., & Jenner, G. A. (1996). Trace element partition coefficients for clinopyroxene and phlogopite in an alkaline lamprophyre from Newfoundland by LAM-ICP-MS. *Geochimica et Cosmochimica Acta*, *60*(4), 629–638. https://doi.org/10.1016/0016-7037(95)00422-X

Font, L., Davidson, J. P., Pearson, D. G., Nowell, G. M., Jerram, D. A., & Ottley, C. J. (2008). Sr and Pb isotope micro-analysis of plagioclase crystals from Skye lavas: An insight into open-system processes in a flood basalt province. *Journal of Petrology*, *49*, 1449–1471. https://doi.org/10.1093/petrology/egn032

Frost, C. D., & Frost, B. R. (2010). On ferroan (A-type) granitoids: Their compositional variability and modes of origin. *Journal of Petrology*, *52*, 39–53.

Frost, B. R., Barnes, C. G., Collins, W. J., Arculus, R. J., Ellis, D. J., & Frost, C. D. (2001). A geochemical classification for granitic rocks. *Journal of Petrology*, *42*(11), 2033–2048. https://doi.org/10.1093/petrology/42.11.2033

Gagnevin, D., Waight, T. E., Daly, J. S., Poli, G., & Conticelli, S. (2007). Insights into magmatic evolution and recharge history in Capraia Volcano (Italy) from chemical and isotopic zoning in plagioclase phenocrysts. *Journal of Volcanology and Geothermal Research*, *168*, 28–54. https://doi.org/10.1016/j.jvolgeores.2007.07.018

Gagnevin, D., Daly, J. S., Horstwood, M. S. A., & Whitehouse, M. J. (2011). In-situ, zircon U−Pb, oxygen and hafnium isotopic evidence for magma mixing and mantle metasomatism in the Tuscan Magmatic Province, Italy. *Earth and Planetary Science Letters*, *305*, 45–56. https://doi.org/10.1016/j.epsl.2011.02.039

Gazel, E., Hayes, J. L., Hoernle, K., Kelemen, P., Everson, E., Holbrook, W. S., & Calvert, A. J. (2015). Continental crust generated in oceanic arcs. *Nature Geoscience*, *8*(4), 321–327. https://doi.org/10.1038/ngeo2392

Geological Bureau of Zhejiang ProvincE (1967). Survey report on regional geology and mineral resources. (H-50-XVII), 107 pp (in Chinese).

Gilder, S. A., Keller, G. R., Ming, L., & Goodell, P. C. (1991). Timing and spatial distribution of rifting in China. *Tectonophysics*, *197*(2-4), 225–243. https://doi.org/10.1016/0040-1951(91)90043-R

Ginibre, C., & Davidson, J. P. (2014). Sr isotope zoning in plagioclase from parinacota volcano (northern chile): quantifying magma mixing and crustal contamination. *Journal of Petrology*, *55*(6), 1203–1238.

Ginibre, C., & Wörner, G. (2007). Variable parent magmas and recharge regimes of the parinacota magma system (in Chile) revealed by Fe, Mg and Sr zoning in plagioclase. *Lithos*, *98*, 118–140. https://doi.org/10.1016/j.lithos.2007.03.004

Glazner, A. F. (2007). Thermal limitations on incorporation of wall rock into magma. *Geology*, *35*(4), 319–322. https://doi.org/10.1130/G23134A.1

González-García, D., Behrens, H., Petrelli, M., Vetere, F., Morgavi, D., Zhang, C., & Perugini, D. (2017). Water-enhanced interdiffusion of major elements between natural shoshonite and high-K rhyolite melts. *Chemical Geology*, https://doi.org/10.1016/j.chemgeo.2017.05.023, *466*, 86–101.

Goolaerts, A., Mattielli, N., de Jong, J., Weis, D., & Scoates, J. S. (2004). Hf and Lu isotopic reference values for the zircon standard 91500 by MC-ICP-MS. *Chemical Geology*, *206*, 1–9. https://doi.org/10.1016/j.chemgeo.2004.01.008

Griffin, W. L., Pearson, N. J., Belousova, E., Jackson, S. E., Achterbergh, E. V., & O'Reilly, S. Y. (2000). The Hf isotope composition of Cratonic mantle: LAM-ICP-MS analysis of zircon megacrysts in kimberlites. *Geochimica et Cosmochimica Acta*, *64*(1), 133–147. https://doi.org/10.1016/S0016-7037(99)00343-9

Griffin, W. L., Wang, X., Jackson, S. E., Pearson, N. J., O'Reilly, S. Y., Xu, X., & Zhou, X. (2002). Zircon chemistry and magma mixing, SE China: In-situ analysis of Hf isotopes, Tonglu and Pingtan igneous complexes. *Lithos*, *61*(3-4), 237–269. https://doi.org/10.1016/S0024-4937(02)00082-8

Guo, Z., Wilson, M., Zhang, M., Cheng, Z., & Zhang, L. (2015). Post-collisional ultrapotassic mafic magmatism in south Tibet: Products of partial melting of pyroxenite in the mantle wedge induced by roll-back and delamination of the subducted Indian continental lithosphere slab. *Journal of Petrology*, *56*(7), 798–804.

Harrison, T. M., Armstrong, R. L., Naeser, C. W., & Harakal, J. E. (1979). Geochronology and thermal history of the coast plutonic complex, near Prince Rupert, British Columbia. *Canadian Journal of Earth Sciences*, *16*(3), 400–410. https://doi.org/10.1139/e79-038

Hawkesworth, C. J., & Kemp, A. I. S. (2006). Evolution of the continental crust. *Nature*, *443*(7113), 811–817. https://doi.org/10.1038/nature05191

He, Z. Y., & Xu, X. S. (2012). Petrogenesis of the late Yanshanian mantle-derived intrusions in southeastern China: Response to the geodynamics of paleo-Pacific plate subduction. *Chemical Geology*, *328*, 208–221. https://doi.org/10.1016/j.chemgeo.2011.09.014

Herzberg, C. (2011). Identification of source lithology in the Hawaiian and Canary Islands: Implications for origins. *Journal of Petrology*, *52*, 113–146. https://doi.org/10.1093/petrology/egq075

Herzberg, C., Cabral, R. A., Jackson, M. G., Vidito, C., Day, J. M. D., & Hauri, E. H. (2014). Phantom Archean crust in Mangaia hotspot lavas and the meaning of heterogeneous mantle. *Earth and Planetary Science Letters*, *396*, 97–106. https://doi.org/10.1016/j.epsl.2014.03.065

Hofmann, A. W. (2003). Sampling mantle heterogeneity through oceanic basalts: Isotopes and trace elements. *Treatise on geochemistry*, *2*, 568.

Hu, G. R. (1998). Study on geological geochemistry, isotopic chronogy and metamorphic *P-T-t* path of metamorphic rock belt in Central Jiangxi, Ph.D. thesis, Nanjing University, China

Hu, Q., Yu, K., Liu, Y., Hu, Z., & Zong, K. (2017). The 131-134 Ma A-type granites from northern Zhejiang Province, South China: Implications for partial melting of the Neoproterozoic lower crust. *Lithos*, *294*, 39–52. https://doi.org/10.1016/j.lithos.2017.09.016

Huang, H. Q., Li, X. H., Li, W. X., & Li, Z. X. (2011). Formation of high $\delta^{18}O$ fayalite-bearing A-type granite by high-temperature melting of granulitic metasedimentary rocks, southern China. *Geology*, *39*, 903–906. https://doi.org/10.1130/G32080.1

Iizuka, T., Komiya, T., Rino, S., Maruyama, S., & Hirata, T. (2010). Detrital zircon evidence for Hf isotopic evolution of granitoid crust and continental growth. *Geochimica et Cosmochimica Acta*, *74*, 2450–2472. https://doi.org/10.1016/j.gca.2010.01.023

Ionov, D. A., Griffin, W. L., & O'Reilly, S. Y. (1997). Volatile-bearing minerals and lithophile trace elements in the upper mantle. *Chemical Geology*, *141*(3-4), 153–184. https://doi.org/10.1016/S0009-2541(97)00061-2

Jackson, S. E., Pearson, N. J., Griffin, W. L., & Belousova, E. A. (2004). The application of laser ablation-inductively coupled plasma-mass spectrometry to in situ U−Pb zircon geochronology. *Chemical Geology*, *211*, 47–69. https://doi.org/10.1016/j.chemgeo.2004.06.017

Jackson, M. G., Hart, S. R., Koppers, A. A., Staudigel, H., Konter, J., Blusztajn, J., … Russell, J. A. (2007). The return of subducted continental crust in Samoan lavas. *Nature*, *448*, 684–687. https://doi.org/10.1038/nature06048

Jacob, K. H., Farmer, G. L., Buchwaldt, R., & Bowring, S. A. (2015). Deep crustal anatexis, magma mixing, and the generation of epizonal plutons in the southern Rocky Mountains, Colorado. *Contributions to Mineralogy and Petrology*, *169*(1), 1–23.

Jahn, B. M. (2004). The Central Asian Orogenic Belt and growth of the continental crust in the Phanerozoic. *Geological Society, London*, *226*, 73–100. https://doi.org/10.1144/GSL.SP.2004.226.01.05

Jahn, B. M., Wu, F., & Chen, B. (2000). Massive granitoid generation in Central Asia: Nd isotope evidence and implication for continental growth in the Phanerozoic. *Episodes*, *23*(2), 82–92.

Jiang, Y. H., Ling, H. F., Jiang, S. Y., Fan, H. R., Shen, W. Z., & Ni, P. (2005). Petrogenesis of a Late Jurassic peraluminous volcanic complex and its high-Mg, potassic, quenched enclaves at Xiangshan, southeast China. *Journal of Petrology*, *46*, 1121–1154. https://doi.org/10.1093/petrology/egi012

Jiang, Y. H., Zhao, P., Zhou, Q., Liao, S. Y., & Jin, G. D. (2011). Petrogenesis and tectonic implications of Early Cretaceous S-and A-type granites in the northwest of the Gan-Hang rift, SE China. *Lithos*, *121*, 55–73. https://doi.org/10.1016/j.lithos.2010.10.001

Kelley, K. A., Plank, T., Grove, T. L., Stolper, E. M., Newman, S., & Hauri, E. (2006). Mantle melting as a function of water content beneath back-arc basins. *Journal of Geophysical Research*, *111*, B09208. https://doi.org/10.1029/2005JB003732

Kessel, R., Schmidt, M. W., Ulmer, P., & Pettke, T. (2005). Trace element signature of subduction-zone fluids, melts and supercritical liquids at 120-180 km depth. *Nature*, *437*, 724–727. https://doi.org/10.1038/nature03971

King, P. L., White, A. J. R., Chappell, B. W., & Allen, C. M. (1997). Characterization and origin of aluminous A-type granites from the Lachlan Fold Belt, southeastern Australia. *Journal of Petrology*, *38*(3), 371–391. https://doi.org/10.1093/petroj/38.3.371

King, P. L., Chappell, B. W., Allen, C. M., & White, A. J. R. (2001). Are A-type granites the high-temperature felsic granites? Evidence from fractionated granites of the Wangrah Suite. *Australian Journal of Earth Sciences*, *48*(4), 501–514. https://doi.org/10.1046/j.1440-0952.2001.00881.x

Kokfelt, T. F., Hoernle, K. A. J., Hauff, F., Fiebig, J., Werner, R., & Garbe-Schoenberg, D. (2006). Combined trace element and Pb-Nd-Sr-O isotope evidence for recycled oceanic crust (upper and lower) in the Iceland mantle plume. *Journal of Petrology*, *47*, 1705–1749. https://doi.org/10.1093/petrology/egl025

Lambart, S., Laporte, D., & Schiano, P. (2009). An experimental study of pyroxenite partial melts at 1 and 1.5 GPa: Implications for the major-element composition of mid-ocean ridge basalts. *Earth and Planetary Science Letters*, *288*, 335–347. https://doi.org/10.1016/j.epsl.2009.09.038

Landenberger, B., & Collins, W. J. (1996). Derivation of A-type granites from a dehydrated charnockitic lower crust: Evidence from the Chaelundi complex, eastern Australia. *Journal of Petrology*, *37*(1), 145–170. https://doi.org/10.1093/petrology/37.1.145

Laumonier, M., Scaillet, B., Pichavant, M., Champallier, R., Andujar, J., & Arbaret, L. (2014). On the conditions of magma mixing and its bearing on andesite production in the crust. *Nature Communications*, *5*, 5607–5607. https://doi.org/10.1038/ncomms6607

Lee, J. K., Williams, I. S., & Ellis, D. J. (1997). Pb, U and Th diffusion in natural zircon. *Nature*, *390*(6656), 159–162. https://doi.org/10.1038/36554

Lesher, C. E. (1990). Decoupling of chemical and isotopic exchange during magma mixing. *Nature*, *344*(6263), 235–237. https://doi.org/10.1038/344235a0

Li, Z. X., & Li, X. H. (2007). Formation of the 1300-km-wide intracontinental orogen and postorogenic magmatic province in Mesozoic south China: A flat-slab subduction model. *Geology*, *35*, 179. https://doi.org/10.1130/G23193A.1

Li, X. H., Li, Z. X., & Li, W. X. (2007). U−Pb zircon, geochemical and Sr-Nd-Hf isotope constraints on age and origin of Jurassic I- and A-type granites from central Guangdong, SE China: A major igneous event in response to foundering of a subducted flat-slab? *Lithos*, *96*, 186–204. https://doi.org/10.1016/j.lithos.2006.09.018

Li, W. X., Li, X. H., Li, Z. X., & Lou, F. S. (2008). Obduction-type granites within the NE Jiangxi ophiolite: Implications for the final amalgamation between the Yangtze and Cathaysia blocks. *Precambrian Research*, *13*, 288–301.

Li, X. H., Li, W. X., Li, Z. X., Lo, C. H., Wang, J., Ye, M. F., & Yang, Y. H. (2009). Amalgamation between the Yangtze and Cathaysia blocks in south China: Constraints from SHRIMP U−Pb zircon ages, geochemistry and Nd-Hf isotopes of the Shuangxiwu volcanic rocks. *Precambrian Research*, *174*, 117–128. https://doi.org/10.1016/j.precamres.2009.07.004

Li, Z., Zhou, J., Mao, J., Santosh, M., Yu, M., Li, Y., … Hu, Y. (2013). Zircon U–Pb geochronology and geochemistry of two episodes of granitoids from the northwestern Zhejiang Province, SE China: Implication for magmatic evolution and tectonic transition. *Lithos*, *179*, 334–352. https://doi.org/10.1016/j.lithos.2013.07.014

Liu, L., Xu, X., & Zou, H. (2012). Episodic eruptions of the late Mesozoic volcanic sequences in southeastern Zhejiang, SE China: Petrogenesis and implications for the geodynamics of paleo-Pacific subduction. *Lithos*, *154*, 166–180. https://doi.org/10.1016/j.lithos.2012.07.002

Liu, L., Xu, X., & Xia, Y. (2014). Cretaceous Pacific plate movement beneath SE China: Evidence from episodic volcanism and related intrusions. *Tectonophysics*, *614*(3), 170–184. https://doi.org/10.1016/j.tecto.2013.12.007

Liu, D., Zhao, Z., Zhu, D. C., Niu, Y., Widom, E., Teng, F. Z., … Mo, X. (2015). Identifying mantle carbonatite metasomatism through Os–Sr–Mg isotopes in Tibetan ultrapotassic rocks. *Earth and Planetary Science Letters*, *430*, 458–469. https://doi.org/10.1016/j.epsl.2015.09.005

Liu, L., Xu, X., & Xia, Y. (2015). Asynchronizing paleo-Pacific slab rollback beneath SE China: Insights from the episodic Late Mesozoic volcanism. *Precambrian Research*, *37*, 397–407.

Liu, X. C., Wu, Y. B., Fisher, C. M., Hanchar, J. M., Beranek, L., Gao, S., & Wang, H. (2017). Tracing crustal evolution by U−Th−Pb, Sm−Nd, and Lu−Hf isotopes in detrital monazite and zircon from modern rivers. *Geology*, *45*(2), 103–106. https://doi.org/10.1130/G38720.1

Lu, C. Z., Gu, M. G., Luo, Y. D., Dong, C. W., & Chen, G. F. (2008). Discovery of the Siling aluminous A-type granite in Hangzhou and its tectonic significance. *Geology in China*, *35*, 392–398. (in Chinese)

Lu, Y. J., Kerrich, R., Mccuaig, T. C., Li, Z. X., Hart, C. J., Cawood, P. A., … Tang, S. H. (2013). Geochemical, Sr–Nd–Pb, and zircon Hf–O isotopic compositions of Eocene–Oligocene shoshonitic and potassic adakite-like felsic intrusions in western Yunnan, SW China: Petrogenesis and tectonic implications. *Journal of Petrology*, *54*(7), 1309–1348. https://doi.org/10.1093/petrology/egt013

Luo, B. J., Zhang, H. F., Xu, W. C., Guo, L., Pan, F. B., & Yang, H. (2015). The Middle Triassic Meiwu batholith, west Qinling, central China: Implications for the evolution of compositional diversity, in a composite batholith. *Journal of Petrology*, *56*(6), 1139–1172. https://doi.org/10.1093/petrology/egv032

Ma, X., Chen, B., & Yang, M. (2013). Magma mixing origin for the Aolunhua porphyry related to Mo-Cu mineralization, eastern Central Asian Orogenic Belt. *Precambrian Research*, *24*(3), 1152–1171.

Ma, X., Meert, J. G., Xu, Z., & Zhao, Z. (2017). Evidence of magma mixing identified in the Early Eocene Caina pluton from the Gangdese Batholith, southern Tibet. *Lithos*, *278*, 126–139.

Ma, L., Jiang, S. Y., Hofmann, A. W., Dai, B. Z., Hou, M. L., Zhao, K. D., & Jiang, Y. H. (2014). Lithospheric and asthenospheric sources of lamprophyres in the Jiaodong Peninsula: A consequence of rapid lithospheric thinning beneath the North China Craton? *Geochimica et Cosmochimica Acta*, *124*, 250–271. https://doi.org/10.1016/j.gca.2013.09.035

Maas, R., Nicholls, I. A., & Legg, C. (1997). Igneous and metamorphic enclaves in the S-type Deddick granodiorite, Lachlan Fold Belt, SE Australia: Petrographic, geochemical and Nd−Sr isotopic evidence for crustal melting and magma mixing. *Journal of Petrology*, *38*(7), 815–841. https://doi.org/10.1093/petroj/38.7.815

Mahood, G. A., & Hildreth, E. W. (1983). Large partition coefficients for trace elements in high-silica rhyolites. *Geochimica et Cosmochimica Acta*, *47*(1), 11–30. https://doi.org/10.1016/0016-7037(83)90087-X

McDonough, W. F., & Sun, S. S. (1995). The composition of the Earth. *Chemical Geology*, *120*(3-4), 223–253. https://doi.org/10.1016/0009-2541(94)00140-4

Menzies, M., & Murthy, V. R. (1980). Nd and Sr isotope geochemistry of hydrous mantle nodules and their host alkali basalts: Implications for local heterogeneities in metasomatically veined mantle. *Earth and Planetary Science Letters*, *46*(3), 323–334. https://doi.org/10.1016/0012-821X(80)90048-5

Mushkin, A., Navon, O., Halicz, L., Hartmann, G., & Stein, M. (2003). The petrogenesis of A-type magmas from the Amram Massif, southern Israel. *Journal of Petrology*, *44*(5), 815–832. https://doi.org/10.1093/petrology/44.5.815

Naldrett, A. J., Wilson, A., Kinnaird, J., & Chunnett, G. (2009). PGE tenor and metal ratios within and below the Merensky Reef, Bushveld Complex: Implications for its genesis. *Journal of Petrology*, *50*, 625–659. https://doi.org/10.1093/petrology/egp015

Namur, O., Charlier, B., Toplis, M. J., Higgins, M. D., Hounsell, V., Liégeois, J. P., & Vander Auwera, J. (2011). Differentiation of tholeiitic basalt to A-type granite in the Sept Iles layered intrusion, Canada. *Journal of Petrology*, *52*, 487–539. https://doi.org/10.1093/petrology/egq088

Papoutsa, A., Pe-Piper, G., & Piper, D. J. (2016). Systematic mineralogical diversity in A-type granitic intrusions: Control of magmatic source and geological processes. *Geological Society of America Bulletin*, *128*(3-4), 487–501. https://doi.org/10.1130/B31245.1

Peccerillo, A., & Taylor, S. R. (1976). Geochemistry of Eocene calc-alkaline volcanic rocks from the Kastamonu area, northern Turkey. *Contributions to Mineralogy and Petrology*, *58*(1), 63–81. https://doi.org/10.1007/BF00384745

Peng, T. P., Wang, Y. J., Jiang, Z. M., Yu, X. B., & Peng, B. X. (2004). $^{40}Ar/^{39}Ar$ geochronology and geochemistry of Cretaceous basaltic rocks for the central and northwestern Jiangxi Province. *Geochimica*, *33*, 447–458. (in Chinese)

Pichavant, M., Martel, C., Bourdier, J. L., & Scaillet, B. (2002). Physical conditions, structure, and dynamics of a zoned magma chamber: Mount Pelée (Martinique, Lesser Antilles Arc). *Journal of Geophysical Research*, *107*(B5), 2093. https://doi.org/10.1029/2001JB000315

Plail, M., Edmonds, M., Woods, A. W., Barclay, J., Humphreys, M. C., Herd, R. A., & Christopher, T. (2018). Mafic enclaves record syn-eruptive basalt intrusion and mixing. *Earth and Planetary Science Letters*, *484*, 30–40. https://doi.org/10.1016/j.epsl.2017.11.033

Plank, T. (2014). The chemical composition of subducting sediments. *Treatise on Geochemistry*, 607–629. https://doi.org/10.1016/B978-0-08-095975-7.00319-3

Poli, G., Tommasini, S., & Halliday, A. N. (1996). Trace element and isotopic exchange during acid-basic magma interaction processes. *Earth and Environmental Science Transactions of the Royal Society of Edinburgh*, *87*(1-2), 225–232. https://doi.org/10.1017/S0263593300006635

Prelević, D., Jacob, D. E., & Foley, S. F. (2013). Recycling plus: A new recipe for the formation of Alpine-Himalayan orogenic mantle lithosphere. *Earth and Planetary Science Letters*, *362*, 187–197. https://doi.org/10.1016/j.epsl.2012.11.035

Price, R. C., Smith, I. E., Stewart, R. B., Gamble, J. A., Gruender, K., & Maas, R. (2016). High-K andesite petrogenesis and crustal evolution: Evidence from mafic and ultramafic xenoliths, Egmont Volcano (Mt. Taranaki) and comparisons with Ruapehu Volcano, North Island, New Zealand. *Geochimica et Cosmochimica Acta*, *185*, 328–357. https://doi.org/10.1016/j.gca.2015.12.009

Pu, W., Gao, J. F., Zhao, K. D., Lin, H. F., & Jiang, S. Y. (2005). Separation method of Rb−Sr, Sm−Nd using DCTA and HIBA. *Journal of Nanjing University (Natural Science)*, *41*, 445–450. (in Chinese)

Qi, Y., Hu, R., Liu, S., Coulson, I. M., Qi, H., Tian, J., … Wang, T. (2012). Geochemical and Sr–Nd–Pb isotopic compositions of Mesozoic diabase dykes from the Gan-Hang Tectonic Belt, south China: Petrogenesis and geodynamic significance. *International Geology Review*, *54*(8), 920–939. https://doi.org/10.1080/00206814.2011.588820

Qi, Y., Hu, R., Liu, S., Coulson, I. M., Qi, H., & Tian, J. (2016). Petrogenesis and geodynamic setting of early cretaceous mafic-ultramafic intrusions, South China: A case study from the Gan-hang Tectonic Belt. *Lithos*, *258*, 149–162.

Ratajeski, K., Glazner, A. F., & Miller, B. V. (2001). Geology and geochemistry of mafic to felsic plutonic rocks in the Cretaceous intrusive suite of Yosemite Valley, California. *Geological Society of America Bulletin*, *113*(11), 1486–1502. https://doi.org/10.1130/0016-7606(2001)113%3C1486:GAGOMT%3E2.0.CO;2

Ratajeski, K., Sisson, T. W., & Glazner, A. F. (2005). Experimental and geochemical evidence for derivation of the El Capitan granite, California, by partial melting of hydrous gabbroic lower crust. *Contributions to Mineralogy and Petrology*, *149*, 713–734. https://doi.org/10.1007/s00410-005-0677-4

Roelofse, F., & Ashwal, L. D. (2012). The lower main zone in the northern limb of the Bushveld Complex—a >1.3 km thick sequence of intruded and variably contaminated crystal mushes. *Journal of Petrology*, *53*, 1449–1476. https://doi.org/10.1093/petrology/egs022

Rudnick, R. L., & Gao, S. (2003). Composition of the continental crust. *Treatise on geochemistry*, *3*, 659.

Schleicher, J. M., Bergantz, G. W., Breidenthal, R. E., & Burgisser, A. (2016). Time scales of crystal mixing in magma mushes. *Geophysical Research Letters*, *43*, 1543–1550. https://doi.org/10.1002/2015GL067372

Shaw, S. E., & Flood, R. H. (2009). Zircon Hf isotopic evidence for mixing of crustal and silicic mantle-derived magmas in a zoned granite pluton, eastern Australia. *Journal of Petrology*, *50*, 147–168.

Shaw, S. E., Flood, R. H., & Pearson, N. J. (2011). The New England batholith of eastern Australia: Evidence of silicic magma mixing from zircon $^{176}Hf/^{177}Hf$ ratios. *Lithos*, *126*, 115–126. https://doi.org/10.1016/j.lithos.2011.06.011

Shorttle, O., Maclennan, J., & Lambart, S. (2014). Quantifying lithological variability in the mantle. *Earth and Planetary Science Letters*, *395*, 24–40. https://doi.org/10.1016/j.epsl.2014.03.040

Shu, X., Yang, S. Y., Jiang, S. Y., & Ye, M. (2017). Petrogenesis and geodynamic setting of Early Cretaceous felsic rocks in the Gan-Hang Belt, southeast China: Constraints from geochronology and geochemistry of the tuffs and trachyandesitic rocks in Shengyuan volcanic basin. *Lithos*, *284-285*, 691–708. https://doi.org/10.1016/j.lithos.2017.05.007

Słaby, E., & Martin, H. (2008). Mafic and felsic magma interaction in granites: The Hercynian Karkonosze pluton (Sudetes, Bohemian Massif). *Journal of Petrology*, *49*, 35.

Sobolev, A. V., Hofmann, A. W., Sobolev, S. V., & Nikogosian, I. K. (2005). An olivine-free mantle source of Hawaiian shield basalts. *Nature*, *434*, 590–597. https://doi.org/10.1038/nature03411

Sobolev, A. V., Hofmann, A. W., Kuzmin, D. V., Yaxley, G. M., Arndt, N. T., Chung, S. L., … Gurenko, A. A. (2007). The amount of recycled crust in sources of mantle-derived melts. *Science*, *316*, 412–417. https://doi.org/10.1126/science.%201138113

Söderlund, U., Patchett, P. J., Vervoort, J. D., & Isachsen, C. E. (2004). The ^{176}Lu decay constant determined by Lu−Hf and U−Pb isotope systematics of Precambrian mafic intrusions. *Earth and Planetary Science Letters*, *219*, 311–324. https://doi.org/10.1016/S0012-821X(04)00012-3

Stelten, M. E., Cooper, K. M., Vazquez, J. A., Reid, M. R., Barfod, G. H., Wimpenny, J., & Yin, Q. Z. (2013). Magma mixing and the generation of isotopic juvenile silicic magma at Yellowstone caldera inferred from coupling ^{238}U-^{230}Th ages with trace elements and Hf and O isotopes in zircon and Pb isotopes in sanidine. *Contributions to Mineralogy and Petrology*, *166*(2), 587–613. https://doi.org/10.1007/s00410-013-0893-2

Stix, J., & Gorton, M. P. (1990). Variations in trace element partition coefficients in sanidine in the Cerro Toledo Rhyolite, Jemez Mountains, New Mexico: Effects of composition, temperature, and volatiles. *Geochimica et Cosmochimica Acta*, *54*(10), 2697–2708. https://doi.org/10.1016/0016-7037(90)90005-6

Stracke, A., & Bourdon, B. (2009). The importance of melt extraction for tracing mantle heterogeneity. *Geochimica et Cosmochimica Acta*, *73*, 218–238. https://doi.org/10.1016/j.gca.2008.10.015

Su, B. X., Qin, K. Z., Sakyi, P. A., Liu, P. P., Tang, D. M., & Malaviarachchi, S. P. K. (2011). Geochemistry and geochronology of acidic rocks in the beishan region, NW China: Petrogenesis and tectonic implications. *Journal of Asian Earth Sciences*, *41*, 31–43. https://doi.org/10.1016/j.jseaes.2010.12.002

Sun, W., Ding, X., Hu, Y. H., & Li, X. H. (2007). The golden transformation of the cretaceous plate subduction in the west Pacific. *Earth and Planetary Science Letters*, *262*, 533–542. https://doi.org/10.1016/j.epsl.2007.08.021

Sun, F., Xu, X., Zou, H., & Xia, Y. (2015). Petrogenesis and magmatic evolution of ~130Ma A-type granites in southeast China. *Journal of Asian Earth Sciences*, *98*, 209–224. https://doi.org/10.1016/j.jseaes.2014.11.018

Tang, G. J., Chung, S. L., Wang, Q., Wyman, D. A., Dan, W., Chen, H. Y., & Zhao, Z. H. (2014). Petrogenesis of a Late Carboniferous diabase dike-granitoid association in the western Tianshan: Response to the geodynamics of oceanic subduction. *Lithos*, *202-203*(4), 85–99. https://doi.org/10.1016/j.lithos.2014.04.010

Taylor, S. R., & McLennan, S. M. (1985). The continental crust: Its composition and evolution.

Tepley, F. J. III, Davidson, J. P., Tilling, R. I., & Arth, J. G. (2000). Magma mixing, recharge and eruption histories recorded in plagioclase phenocrysts from El Chichón volcano, Mexico. *Journal of Petrology*, *41*(9), 1397–1411. https://doi.org/10.1093/petrology/41.9.1397

Tomlinson, K. Y., Davis, D. W., Percival, J. A., Hughes, D. J., & Thurston, P. C. (2002). Mafic to felsic magmatism and crustal recycling in the Obonga Lake greenstone belt, western Superior Province: Evidence from geochemistry, Nd isotopes and U−Pb geochronology. *Precambrian Research*, *114*(3-4), 295–325. https://doi.org/10.1016/S0301-9268(01)00232-7

Ubide, T., Gal, C., Larrea, P., Arranz, E., Lago, M., & Tierz, P. (2014). The relevance of crystal transfer to magma mixing: A case study in composite dykes from the central pyrenees. *Journal of Petrology*, *55*(8), 1535–1559. https://doi.org/10.1093/petrology/egu033

Vernon, R. H. (2007). Problems in identifying restite in S-type granites of southeastern Australia, with speculations on sources of magma and enclaves. *The Canadian Mineralogist*, *45*, 147–178. https://doi.org/10.2113/gscanmin.45.1.147

Waight, T. E., Wiebe, R. A., & Krogstad, E. J. (2007). Isotopic evidence for multiple contributions to felsic magma chambers: Gouldsboro granite, coastal Maine. *Lithos*, *93*, 234–247. https://doi.org/10.1016/j.lithos.2006.03.066

Wang, Q., Li, J. W., Jian, P., Zhao, Z. H., Xiong, X. L., Bao, Z. W., & Ma, J. L. (2005). Alkaline syenites in eastern Cathaysia (south China): Link to Permian–Triassic transtension. *Earth and Planetary Science Letters*, *230*, 339–354. https://doi.org/10.1016/j.epsl.2004.11.023

Wang, X. L., Zhao, G., Zhou, J. C., Liu, Y., & Hu, J. (2008a). Geochronology and Hf isotopes of zircon from volcanic rocks of the Shuangqiaoshan group, south China: Implications for the Neoproterozoic tectonic evolution of the eastern Jiangnan orogen. *Precambrian Research*, *14*, 355–367.

Wang, X., Wang, T., Haapala, I., & Mao, J. (2008b). *P-T* conditions of crystallization and origin of plagioclase-mantled alkali feldspar megacrysts in the Mesozoic granitoids in the Qinling orogen (China). *Lithos*, *103*, 289–308. https://doi.org/10.1016/j.lithos.2007.09.020

Wang, T., Jahn, B. M., Kovach, V. P., Tong, Y., Hong, D. W., & Han, B. F. (2009). Nd−Sr isotopic mapping of the Chinese Altai and implications for continental growth in the Central Asian Orogenic Belt. *Lithos*, *110*, 359–372. https://doi.org/10.1016/j.lithos.2009.02.001

Wang, G. G., Ni, P., Yao, J., Wang, X. L., Zhao, K. D., Zhu, R. Z., … Zhang, Y. H. (2015). The link between subduction-modified lithosphere and the giant Dexing porphyry copper deposit, South China: Constraints from high-Mg adakitic rocks. *Ore Geology Reviews*, *67*, 109–126. https://doi.org/10.1016/j.oregeorev.2014.12.004

Wenner, J. M., & Coleman, D. S. (2004). Magma mixing and Cretaceous crustal growth: Geology and geochemistry of granites in the central Sierra Nevada batholith, California. *International Geology Review*, *46*, 880–903. https://doi.org/10.2747/0020-6814.46.10.880

Whalen, J. B., Currie, K. L., & Chappell, B. W. (1987). A-type granites: Geochemical characteristics, discrimination and petrogenesis. *Contributions to Mineralogy and Petrology*, *95*(4), 407–419. https://doi.org/10.1007/BF00402202

Wong, J., Sun, M., Xing, G., Li, X. H., Zhao, G., & Wong, K. (2009). Geochemical and zircon U−Pb and Hf isotope study of the Baijuhuajian metaluminous A-type granite: Extension at 125-100 Ma and its tectonic significance for south China. *Lithos*, *112*, 289–305. https://doi.org/10.1016/j.lithos.2009.03.009

Workman, R. K., & Hart, S. R. (2005). Major and trace element composition of the depleted MORB mantle (DMM). *Earth and Planetary Science Letters*, *231*, 53–72. https://doi.org/10.1016/j.epsl.2004.12.005

Wright, J. B. (1969). A simple alkalinity ratio and its application to questions of non-orogenic granite genesis. *Geological Magazine*, *106*(04), 370–384. https://doi.org/10.1017/S0016756800058222

Wu, F. Y., Ji, W. Q., Sun, D. H., Yang, Y. H., & Li, X. H. (2012). Zircon U−Pb geochronology and Hf isotopic compositions of the Mesozoic granites in southern Anhui province, China. *Lithos*, *150*, 6–25. https://doi.org/10.1016/j.lithos.2012.03.020

Xia, Y., Xu, X., Zhao, G., & Liu, L. (2015). Neoproterozoic active continental margin of the Cathaysia block: Evidence from geochronology, geochemistry, and Nd–Hf isotopes of igneous complexes. *Precambrian Research*, *269*, 195–216. https://doi.org/10.1016/j.precamres.2015.08.006

Xia, Y., Xu, X., & Liu, L. (2016). Transition from adakitic to bimodal magmatism induced by the paleo-Pacific plate subduction and slab rollback beneath SE China: Evidence from petrogenesis and tectonic setting of the dyke swarms. *Lithos*, *244*, 182–204. https://doi.org/10.1016/j.lithos.2015.12.006

Xia, Y., Xu, X., Niu, Y., & Liu, L. (2017). Neoproterozoic amalgamation between Yangtze and Cathaysia blocks: The magmatism in various tectonic settings and continent-arc-continent collision. *Precambrian Research*. https://doi.org/10.1016/j.precamres.2017.02.020

Xiang, Y. X., Yang, J. H., Chen, J. Y., & Zhang, Y. (2017). Petrogenesis of Lingshan highly fractionated granites in the southeast China: Implication for Nb–Ta mineralization. *Ore Geology Reviews*, *89*, 495–525. https://doi.org/10.1016/j.oregeorev.2017.06.029

Xu, M., & Tang, H. (2017). Plagioclase crystallisation in a granodioritic melt and its petrogenetic implications for the origin of the A-type granite in east Junggar, NW China. *Geological Journal*. https://doi.org/10.1002/gj.2935

Xu, X., Dong, C., Li, W., & Zhou, X. (1999). Late Mesozoic intrusive complexes in the coastal area of Fujian, SE China: The significance of the gabbro-diorite-granite association. *Lithos*, *46*(2), 299–315. https://doi.org/10.1016/S0024-4937(98)00087-5

Xu, W., Gao, S., Wang, Q., Wang, D., & Liu, Y. (2006). Mesozoic crustal thickening of the eastern North China Craton: Evidence from eclogite xenoliths and petrologic implications. *Geology*, *34*, 721–724. https://doi.org/10.1130/G22551.1

Xu, X., O'Reilly, S. Y., Griffin, W. L., Wang, X., Pearson, N. J., & He, Z. (2007). The crust of Cathaysia: Age, assembly and reworking of two terranes. *Precambrian Research*, *158*, 51–78. https://doi.org/10.1016/j.precamres.2007.04.010

Yang, J. H., Chung, S. L., Zhai, M. G., & Zhou, and X. H. (2004). Geochemical and Sr–Nd–Pb isotopic compositions of mafic dikes from the Jiaodong peninsula, China: Evidence for vein-plus-peridotite melting in the lithospheric mantle. *Lithos*, *73*, 145–160. https://doi.org/10.1016/j.lithos.2003.12.003

Yang, J., Gao, S., Chen, C., Tang, Y., Yuan, H., Gong, H., & Wang, J. (2009). Episodic crustal growth of north China as revealed by U−Pb age and Hf isotopes of detrital zircons from modern rivers. *Geochimica et Cosmochimica Acta*, *73*, 2660–2673. https://doi.org/10.1016/j.gca.2009.02.007

Yang, S. Y., Jiang, S. Y., Zhao, K. D., Jiang, Y. H., Ling, H. F., & Luo, L. (2012). Geochronology, geochemistry and tectonic significance of two Early Cretaceous A-type granites in the Gan-Hang belt, southeast China. *Lithos*, *150*, 155–170. https://doi.org/10.1016/j.lithos.2012.01.028

Yang, S. H., Maier, W. D., Lahaye, Y., & O'Brien, H. (2013). Strontium isotope disequilibrium of plagioclase in the upper critical zone of the Bushveld Complex: Evidence for mixing of crystal slurries. *Contributions to Mineralogy and Petrology*, *166*(4), 959–974. https://doi.org/10.1007/s00410-013-0903-4

Yang, W.-B., Niu, H.-C., Hollings, P., Zurevinski, S. E., & Li, N.-B. (2017). The role of recycled oceanic crust in the generation of alkaline A-type granites. *Journal of Geophysical Research: Solid Earth*, *122*, 9775–9783. https://doi.org/10.1002/2017JB014921

Yang, Y. H., Zhang, H. F., Chu, Z. Y., Xie, L. W., & Wu, F. Y. (2010). Combined chemical separation of Lu, Hf, Rb, Sr, Sm and Nd from a single rock digest and precise and accurate isotope determinations of Lu–Hf, Rb–Sr and Sm–Nd isotope systems using Multi-collector ICP-MS and TIMS. *International Journal of Mass Spectrometry*, *290*, 120–126. https://doi.org/10.1016/j.ijms.2009.12.011

Yu, X. Q., Shu, L. S., & Yan, T. Z. (2004). Geochemistry and its tectonic significance for basalts of late period Of Early Cretaceous from Jiangshan-Guangfeng, SE China. *Geochimica*, *33*, 465–476. (in Chinese with English abstract)

Yuan, Z. X., Wu, L. S., Zhang, Z. Q., & Ye, X. J. (1991). The Sm−Nd, Rb−Sr isotopic age-dating of Mayuan group in northern Fujian. *Acta Petrologica et Mineralogica*, *10*(2), 127–132. (in Chinese)

Zeng, G., He, Z. Y., Li, Z., Xu, X. S., & Chen, L. H. (2016). Geodynamics of paleo-Pacific plate subduction constrained by the source lithologies of Late Mesozoic basalts in southeastern China. *Geophysical Research Letters*, *43*, 10,189–10,197. https://doi.org/10.1002/2016GL070346

Zeng, G., Chen, L. H., Yu, X., Liu, J. Q., Xu, X. S., & Erdmann, S. (2017). Magma-magma interaction in the mantle beneath eastern China. *Journal of Geophysical Research: Solid Earth*, *122*, 2763–2779. https://doi.org/10.1002/2017JB014023

Zhang, G. L., Zong, C. L., Yin, X. B., & Li, H. (2012). Geochemical constraints on a mixed pyroxenite-peridotite source for East Pacific Rise basalts. *Chemical Geology*, *330*, 176–187.

Zhang, J., Wang, T., Castro, A., Zhang, L., Shi, X., Tong, Y., … Iaccheri, L. M. (2016). Multiple mixing and hybridization from magma source to final emplacement in the Permian Yamatu pluton, the Northern Alxa Block, China. *Journal of Petrology*, *57*(5), 933–980. https://doi.org/10.1093/petrology/egw028

Zhao, L., Guo, F., Fan, W., Zhang, Q., Wu, Y., Li, J., & Yan, W. (2016). Early Cretaceous potassic volcanic rocks in the Jiangnan Orogenic Belt, East China: Crustal melting in response to subduction of the Pacific–Izanagi ridge? *Chemical Geology*, *437*, 30–43. https://doi.org/10.1016/j.chemgeo.2016.05.011

Zhao, J. L., Qiu, J. S., Liu, L., & Wang, R. Q. (2016). The Late Cretaceous I- and A-type granite association of southeast China: Implications for the origin and evolution of post-collisional extensional magmatism. *Lithos*, *240*, 16–33.

Zhong, H., Campbell, I. H., Zhu, W. G., Allen, C. M., Hu, R. Z., Xie, L. W., & He, D. F. (2011). Timing and source constraints on the relationship between mafic and felsic intrusions in the Emeishan large igneous province. *Geochimica et Cosmochimica Acta*, *75*, 1374–1395. https://doi.org/10.1016/j.gca.2010.12.016

Zhou, J. (2016). Petrogenesis of the Early Cretaceous granitiods in northwestern Zhe-jiang and its tectonic evolution, PhD thesis, Zhejiang University, China.

Zhou, X. M., & Li, W. X. (2000). Origin of Late Mesozoic igneous rocks in southeastern China: Implications for lithosphere subduction and underplating of mafic magmas. *Tectonophysics*, *326*(3-4), 269–287. https://doi.org/10.1016/S0040-1951(00)00120-7

Zhou, X. M., Sun, T., Shen, W. Z., Shu, L. S., & Niu, Y. L. (2006). Petrogenesis of Mesozoic granitoids and volcanic rocks in South China: A response to tectonic evolution. *Episodes*, *29*, 26–33.

Zhou, J., Jiang, Y. H., Xing, G., Zeng, Y., & Ge, W. (2013). Geochronology and petrogenesis of Cretaceous A-type granites from the NE Jiangnan Orogen, SE China. *International Geology Review*, *55*(11), 1359–1383. https://doi.org/10.1080/00206814.2013.774199